CASL-U-2019-1870-000 Rev.0

ATF material model development and validation for priority fuel concepts L3:FMC.FUEL.P19.06

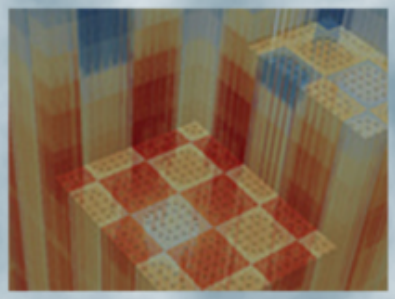

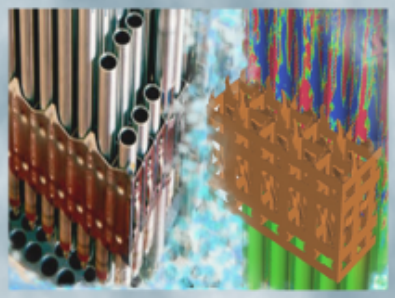


K. A. Gamble, INL
G. Pastore, INL
M. W. D. Cooper, LANL
D. Andersson, LANL

July 30, 2019

U.S. DEPARTMENT OF ENERGY | Nuclear Energy

REVISION LOG

Revision	Date	Affected Pages	Revision Description

Document pages that are:

Export Controlled _____NONE_____

IP/Proprietary/NDA Controlled_____NONE_____

Sensitive Controlled_____NONE_____

Requested Distribution:

To: FMC FA Lead

Copy: CASL PM

ATF material model development and validation for priority fuel concepts

K. A. Gamble
G. Pastore

Fuel Modeling and Simulation
Idaho National Laboratory
P.O. Box 1625
Idaho Falls, ID 83415-3840, USA

M. W. D. Cooper
D. Andersson

MST-8, Materials Science in Radiation and Dynamics Extremes
Las Alamos National Laboratory
P.O. Box 1663
Las Alamos, NM 87545, USA

July 30, 2019

Contents

1 Introduction

Development, implementation, and validation of material and behavior models for accident tolerant fuel (ATF) concepts in the Bison fuel performance code began in 2014 in response to the events that occurred at the Fukushima Daichii nuclear power plant in March 2011. Early on the focus was on U_3Si_2 fuel and FeCrAl cladding as part of a high impact problem through the Nuclear Energy and Advanced Modeling Simulation (NEAMS) program. Then, developments for Cr_2O_3-doped UO_2 fuel, and SiC-SiC and Cr-coated zirconium-based claddings began based upon industry interests. In late fiscal year 2018 the Consortium for Advanced Simulation of Light Water Reactors (CASL) took over further ATF work in Bison in support of the Nuclear Regulatory Commission (NRC) engagement. Discussions with the NRC identified their list of priority fuel and cladding concepts, which included Cr_2O_3-doped UO_2 and U_3Si_2 fuels, and Cr-coated zirconium-based and FeCrAl claddings. In particular, the NRC suggested that reports similar in form to NUREG/CR-7024 [1] that was developed for traditional LWR materials UO_2 and zirconium-based claddings (i.e., Zircaloy-4, M5®, ZIRLO™) be created for the priority ATF concepts.

The approach to ATF capability development in Bison since the beginning has been two-fold: (1) empirical correlations and (2) multiscale model development. Both approaches have uncertainty inherent to them. Uncertainty in empirical correlations is bounded by the experimental data upon which with the correlation was developed. Models developed through a multiscale approach have uncertainty associated with the lower length scale calculations and input parameters that must be propagated to the engineering scale model in Bison. In this report, the recommended models, their range of applicability (e.g., temperature, burnup), and associated uncertainty for the NRC priority fuel concepts Cr_2O_3-doped UO_2 and U_3Si_2 are presented in a manner similar to the aforementioned NUREG. In addition, the Cr_2O_3-doped UO_2 models are validated to the Halden Reactor tess IFA-677.1 rods 1 and 5 and IFA-716.1 rod 1. For U_3Si_2 the models are validated to the recent post-irradiation examination (PIE) data ATF-13 and ATF-15 rods that were irradiated in the Advanced Test Reactor (ATR) at Idaho National Laboratory [2]. Finally, an uncertainty quantification (UQ) and sensitivity analysis (SA) is completed on a single rod for each fuel concept that takes into account the defined uncertainty in select models. The results of the UQ and SA analyses indicate that given the large uncertainty in some of the input ATF models that the uncertainty on the Bison predictions of fuel performance metrics of interest bound the available experimental data. Correlation coefficients are also reported that identified the uncertain inputs with the strongest correlation (positive or negative) with the outputs of interest. Fuel performance metrics investigated include fuel elongation, rod internal pressure, fuel centerline temperature, and fission gas release.

2 Cr_2O_3-doped UO_2

Cr_2O_3-doped UO_2 fuel is a potentially attractive alternative to traditional UO_2 fuel currently used in LWRs because of its larger grain size possibly reducing fission gas release. A potential advantage in terms of Pellet-Cladding Interaction (PCI) behavior also exists, which is related to different creep and cracking behaviors relative to standard UO_2. Material models used in analyses of Cr_2O_3-doped UO_2 fuel with the Bison fuel performance code are described in the following subsections including a description of how the correlation or model was developed, the applicability of the model, and its associated uncertainty. Many of the models used are the same as UO_2 given the similarities in the fuel type. If the model is empirical in nature the uncertainty is derived from the experimental data upon which the model was created and in the case of multiscale developed models the uncertainty in the lower length scale calculations and parameters are propagated to the engineering scale. The name of the C++ class that computes the respective properties within Bison is listed in parentheses in the subsection header. The details described below can also be found in the online theory and user documentation packaged with the Bison code.

2.1 Thermal Properties (`ThermalFuel`)

2.1.1 Models Choice

Thermal Conductivity Model

The effect of doping on the thermal conductivity of UO_2 has been discussed in detail in [3]. The addition of Cr (or other dopants) could modify the thermal conductivity of fresh fuel, either by defect-phonon scattering or by forming a secondary phase with a different thermal conductivity to UO_2. In [4] the thermal diffusivity of Cr_2O_3/Al_2O_3 doped UO_2 was measured and only a small change was noted compared to undoped UO_2, indicating that dopants in small additions will have limited impact on thermal conductivity. However, the full data set was not provided. Any impact on thermal conductivity is expected to be most significant at the beginning of life, while its effect may be washed out with burnup due to the accumulation of fission products in the UO_2 lattice. The larger grain size of Cr_2O_3-doped UO_2 compared to pure UO_2 is expected to have a negligible effect on thermal conductivity, given that grain size must be on the submicron scale to impact thermal transport noticeably [5].

Based on the information available at this time, therefore, it appears that considering a negligible effect of the Cr_2O_3 dopant on the thermal conductivity is a suitable assumption. In this work, the Halden thermal conductivity correlation for pure UO_2 has been used to represent the thermal conductivity of Cr_2O_3-doped UO_2. This correlation was also used by the Halden Project in fuel temperature calculations for Cr_2O_3-doped UO_2 fuel rod experiments, see [6]. No effect of the Cr_2O_3 doping on fuel thermal conductivity was assumed (while a significant increase of fuel thermal conductivity in the case of BeO dopant was pointed out) [6].

According to the Halden correlation, the thermal conductivity for 95% theoretical density UO_2 is given by

$$k_{95} = \frac{1.0}{0.1148 + 1.1599Gd + 1.1599 f_x + 4\times10^{-3}Bu + 2.475\times10^{-4}\left(1.0 - 3.33\times10^{-3}Bu\right)\cdot\min\left(1650, T_c\right)} + \\ +1.32\times10^{-2}\exp\left(0.00188T_c\right) \quad (1)$$

where k_{95} is the thermal conductivity in W/m-K, T_c the temperature in °C, Bu the burnup in MWd/kgU, Gd the gadolinia concentration in weight percent, and f_x is the deviation from stoichiometry (i.e., (2.0 − oxygen/metal ratio).

Eq. 1 is first multiplied by the appropriate factor to return the thermal conductivity to a density of 100% theoretical density (TD) and then multiplied by a density correction factor to provide a thermal conductivity representative of the material of interest

$$k = k_{95}\cdot 1.0789\cdot\frac{d}{(1 + 0.5\cdot(1-d))} \quad (2)$$

where d is the fuel density in fraction of TD. The multiplier 1.0789 is the inverse of the density correction factor evaluated at 0.95 TD. Fig. 1 illustrates the thermal conductivity model as a function of temperature at various burnups for 95% TD UO_2.

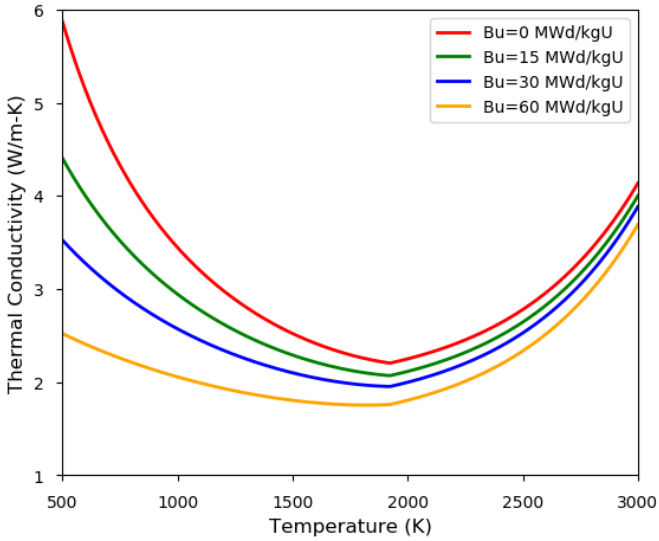

Figure 1: Halden model for thermal conductivity of UO_2 at 95% theoretical density

Specific Heat Model

As reviewed in [3], several experiments have been carried out to determine the effect of Cr_2O_3 or Al_2O_3/Cr_2O_3 doping on the specific heat capacity of UO_2 [4, 7]. Measurements on the ADOPT Westinghouse pellets indicated negligible impact on the specific heat, as all data was within the 3% of the Fink data [4, 8]. In ref. [7], reference is made to experiments carried out at JRC-ITU where negligible impact was noted due to Cr_2O_3 doping, i.e., within the statistical error of the equipment and in line with rule of mixtures. Therefore, it is not expected that the dopant will have a significant impact on the specific heat of the fuel compared to undoped UO_2.

Based on the evidence discussed above, the correlation for specific heat of pure UO_2 in Bison is used in this work to represent the specific heat of Cr_2O_3-doped UO_2. The correlation is from [8] and reads:

$$C_p = 52.1743 + 87.951t + 84.2411t^2 + 31542t^3 - 2.6334t^4 - 0.71391t^{-2} \quad (3)$$

where $t = T/1000$ and T is the temperature in K. For conversion of C_p from units of J/mol-K to J/kg-K the value obtained by the correlation above is divided by 0.27.

2.1.2 Applicability and Uncertainty

The Halden UO_2 thermal conductivity correlation is valid over the following ranges [9]

$300 \leq T \leq 3000K$
$0 \leq Bu \leq 62MWd/kgU$
$0.92 \leq d \leq 0.97$
$0 \leq Gd \leq 10$ wt.%

Under the assumption that the Cr_2O_3 dopant has a negligible effect, the modeling uncertainty for the thermal conductivity of Cr_2O_3-doped UO_2 is estimated in this work based on the uncertainty pertaining to the thermal conductivity of pure UO_2. In [10], an uncertainty of ±10% (independent of the temperature) for the fuel thermal conductivity is assumed. The uncertainty range for the UO_2 thermal conductivity in [10] was determined based on the data from [11] and the recommendations in the FRAPCON-3.4 manual [12]. An uncertainty range of ±10% for the thermal conductivity of UO_2 also appears consistent with the evaluations found in refs. [1] and [13].

Based on the current knowledge as overviewed above, in this work an uncertainty range of ±10% is proposed for the thermal conductivity of Cr_2O_3-doped UO_2. This is assumed as the 95% confidence interval of a Gaussian distribution for the thermal conductivity [10].

The uncertainty in the heat capacity of UO_2 was estimated in [13] as ±2% from 298 to 1800 K, and ±13% from 1800 to the melting point.

2.2 Thermal Expansion (`UO2ThermalExpansionEigenstrain`)

2.2.1 Model Choice

The potential impact of doping on the coefficient of thermal expansion of UO_2 has been reviewed in [3]. The thermal expansion coefficient has been shown to be relatively unaffected by the addition of Gd up to 10 wt% [14] and when doping with fission products [15]. Measurements on Cr_2O_3/Al_2O_3 co-doped UO_2 indicate that the change in the thermal expansion coefficient compared to UO_2 is within error [4]. Therefore, it is expected that the thermal expansion coefficient will be similar for doped UO_2 compared to undoped UO_2.

On this basis, the thermal expansion behavior of Cr_2O_3-doped UO_2 is assumed to be analogous to pure UO_2 for modeling purposes. In this work, the strain due to thermal expansion of Cr_2O_3-doped UO_2 is calculated in Bison using a UO_2 correlation, in particular, the MATPRO `FTHEXP` [16] model. The equation for the thermal expansion as a function of the temperature according to the `FTHEXP` model is

$$\frac{\Delta L}{L_0} = K_1 T - K_2 + K_3 \, exp\left(\frac{-E_D}{kT}\right) \tag{4}$$

where $\Delta L / L_0$ (/) is the linear strain due to thermal expansion, T (K) the temperature, E_D (J) the defect formation energy, k (J/K) the Boltzmann constant, and K_1 (K^{-1}), K_2 (/), K_3 (/) are constants. Values for the model paramaters are given in Table 1.

Table 1: Values for the parameters used in the UO_2 thermal expansion model in Bison [16].

Constant	Value	Units
E_D	6.9×10^{-20}	J
K_1	1.0×10^{-5}	K^{-1}
K_2	3.0×10^{-3}	/
K_3	4.0×10^{-2}	/

2.2.2 Applicability and Uncertainty

The fuel thermal expansion correlation used in the `FTHEXP` model is applicable through the melting temperature of UO_2 (∼3113 K).

As mentioned in [1], the uncertainty in the data used to derive the `FTHEXP` model was found to be temperature dependent, increasing approximately linearly with temperature. Therefore, a percentage uncertainty is given rather than a fixed number. In [10], an uncertainty of ±15% (independent of the temperature) for the coefficient of thermal expansion is assumed. The uncertainty range for the UO_2 coefficient of thermal expansion in [10] was determined based on the data from [11] and the recommendations in the FRAPCON-3.4 manual [12].

On this basis, and considering a behavior for Cr_2O_3-doped UO_2 analogous to UO_2 as discussed in Section 2.2.1, in this work an uncertainty range of ±15% is proposed for the coefficient of thermal expansion of Cr_2O_3-doped UO_2. This is assumed as the 95% confidence interval of a Gaussian distribution for the coefficient of thermal expansion [10].

2.3 Grain Size (GrainRadiusAux)

When a polycrystalline material is subject to high temperatures, larger grains tend to grow at the expense of the smaller ones. As a consequence, the latter gradually disappear, thus reducing the total number of grains per unit volume and increasing the average grain size. This phenomenon is known as grain growth. The granular structure of the fuel affects physical processes such as fission gas behavior (see Section 2.4). In Cr_2O_3-doped UO_2, the initial grain size ($\sim$40-70μm) is significantly higher than in pure UO_2 ($\sim$10μm).

2.3.1 Model Choice

The model from Ainscough et al. [17] is implemented in Bison for calculating grain growth in UO_2 fuel. The same model is applied to Cr_2O_3-doped UO_2 in this work. According to this model, the kinetics of grain growth is described by the equation:

$$\frac{dl_{gr}}{dt} = K\left(\frac{1}{l_{gr}} - \frac{1}{l_{gr,lim}}\right) \tag{5}$$

where l_{gr} (μm) is the 2-dimensional (linear intercept) average grain diameter, t (h) the time, K (μm^2/h) the rate constant, which is $5.24 \cdot 10^7 \exp\left(-2.67 \cdot 10^5/(RT)\right)$ for $R = 8.314$ J/(mol·K), and $l_{gr,lim}$ (μm) is the limiting grain size. The latter is a function of temperature such that

$$l_{gr,lim} = 2.23 \cdot 10^3 \exp(-7620/T) \tag{6}$$

Grain shrinkage is not allowed for in the model, i.e., the grain size can only increase or remain constant. The 3-dimensional grain diameter is calculated as $r_{gr} = 1.56\, l_{gr}$ [18].

The large initial grain size for Cr_2O_3-doped UO_2 means that the initial grain size could exceed the limiting grain size even at 1800 K ($l_{gr,lim} = 32\mu m$). Therefore, it is expected that the calculated grain size remains largely constant throughout the irradiation. This is considered acceptable in the absence of specific information on grain growth behavior in Cr_2O_3-doped UO_2.

2.3.2 Applicability and Uncertainty

The data used to derive the model for grain growth applied in this work cover temperatures up to 1773 K [17]. It is therefore assumed that the model is applicable up to 1773 K. However, applicability to Cr_2O_3-doped UO_2 still needs confirmation.

As for the uncertainty in the grain size evolution in UO_2, Van Uffelen et al. [19] reported different estimates for the grain growth kinetic coefficient in UO_2, showing a scatter of about 3 orders of magnitude in the available data. Botazzoli [20] compared several UO_2 grain growth models to a large amount of experimental data from the literature. His study pointed out that the ratio of predicted to experimental grain size is characterized by mean $\mu \approx 1$ and standard deviation $\sigma \approx 0.3$ for all considered models, including the model used in the present work (Eq. 5). On this basis, assuming a normal distribution, the approximate uncertainty in the calculated grain radius was estimated in [21] as $\pm 2\sigma \approx \pm 0.6$. Further investigation is needed to obtain a better estimate of the uncertainty specific to grain size evolution in Cr_2O_3-doped UO_2.

2.4 Fission Gas Behavior (Sifgrs)

The Bison fission gas model incorporates the fundamental physical mechanisms of fission gas behavior and calculates the coupled fission gas release (FGR) and gaseous swelling concurrently. The fundamental physical processes that underlie fission gas behavior in irradiated UO_2 may be outlined as follows. Fission gas atoms generated in the fuel grains diffuse towards grain boundaries through repeated trapping in and irradiation-induced resolution from intra-granular gas bubbles. On the grain boundaries, inter-granular bubbles nucleate and grow as a result of the inflow of gas

atoms from within the grains and the absorption of vacancies from the grain boundaries, giving rise to grain-boundary swelling. Bubble growth brings about bubble coalescence and inter-connection, eventually leading to the formation of a tunnel network through which a fraction of the gas is released to the fuel rod free volume (FGR).

The Bison model was originally developed for pure UO_2 and has been extended to account for the specificities of Cr_2O_3-doped UO_2 in the present work. Specificities include (1) the effect of a larger grain size and (2) an enhanced diffusivity of gas atoms in the lattice due to the dopant.

The grain size affects the fission gas behavior in two ways, i.e., (i) increasing the average diffusion distance for gas atoms in the grains, which reduces the rate of gas transport to the grain boundaries and ultimately FGR and (ii) reducing the grain surface to volume ratio, hence the capacity of the grain faces to store fission gas. Both of these effects are considered naturally in the Bison fission gas model, as it directly describes the grain radius dependent intra-granular and grain-boundary processes. To this end, in Bison the fission gas behavior model is coupled to the grain growth model described in Section 2.3.

To account for the enhanced diffusivity of gas atoms as a result of the doping a multiscale approach was adopted, whereby the Bison model is informed with diffusivities calculated at the lower length scale. The lower length scale calculations were performed at Los Alamos National Laboratory.

In the following, first, the general characteristics of the Bison fission gas model are described (Section 2.4.1), before giving an account of the specific developments for Cr_2O_3-doped UO_2 (Section 2.4.2).

2.4.1 Engineering Model Development

Fission gas transport from within the fuel grains (assumed to be spherical) to the grain boundaries is computed via numerical solution of the relevant diffusion equation in spherical geometry

$$\frac{\partial \mathrm{C_{ig}}}{\partial t} = \frac{b}{b+g} D \nabla^2 \mathrm{C_{ig}} + \beta \tag{7}$$

where $\mathrm{C_{ig}}$ (at $\mathrm{m^{-3}}$) is the intra-granular gas concentration, t (s) the time, g ($\mathrm{s^{-1}}$) the rate of gas atoms trapping into intra-granular bubbles, b ($\mathrm{s^{-1}}$) the rate of gas atom resolution from bubbles back into the lattice, D ($\mathrm{m^2\ s^{-1}}$) the intra-granular single atom diffusion coefficient, and β (at $\mathrm{m^{-3}\ s^{-1}}$) the gas generation rate. The term $b/(b+g)\ D$ represents the effective intra-granular diffusion coefficient [22].

The following correlation is adopted for calculating the intra-granular gas atom diffusion coefficient in standard UO_2 [23, 24]

$$\begin{aligned} D &= D_1 + D_2 + D_3 \\ D_1 &= 7.6 \times 10^{-10} \exp\left(-4.86 \times 10^{-19} \big/ (kT)\right) \\ D_2 &= 4 \times 1.41 \times 10^{-25} \sqrt{F} \exp\left(-1.91 \times 10^{-19} \big/ (kT)\right) \\ D_3 &= 8 \times 10^{-40} F \end{aligned} \tag{8}$$

where D_1 ($\mathrm{m^2 s^{-1}}$) represents intrinsic thermal diffusion, D_2 ($\mathrm{m^2 s^{-1}}$) represents irradiation-enhanced diffusion, k ($\mathrm{JK^{-1}}$) the Boltzmann constant, T (K) the temperature, and F ($\mathrm{m^{-3} s^{-1}}$) the fission rate.

Based on Ham's [25] theory for diffusion-limited precipitation at spherical particles, the trapping rate, g, can be calculated as

$$g = 4\pi D R N \tag{9}$$

where R (m) the mean radius of intra-granular bubbles and N ($\mathrm{m^{-3}}$) the bubble number density. The expression adopted for the resolution rate, b, is the one from [26], which is a slight modification of Turnbull's [27]

$$b = 3.03 F \pi l_f \left(R + Z_0\right)^2 \tag{10}$$

where l_f (m) the length of a fission fragment track and Z_0 (m) the radius of influence of a fission fragment track. The generation rate of fission gas is calculated as

$$\beta = YF \tag{11}$$

where Y (/) is the total yield of fission gas atoms.

The grain-boundary gas behavior analysis involves the calculation of both fission gas swelling and release through a direct description of the intra-granular bubble development. Grain-boundary bubble growth (or shrinkage) is calculated through

$$\frac{dV_{gf}}{dt} = \omega \frac{dn_g}{dt} + \Omega \frac{dn_v}{dt} \tag{12}$$

where V_{gf} (m^3) is the bubble volume, ω (m^3) the Van der Waals' volume of a fission gas atom, n_g (-) the number of fission gas atoms per bubble, Ω (m^3) the atomic (vacancy) volume in the bubble, and n_v (-) the number of vacancies per bubble. The gas atom inflow rate at the bubble, dn_g/dt, is obtained from Eq. 7. The vacancy absorption/emission rate at the bubble, dn_v/dt, is calculated using the following model [28]

$$\frac{dn_v}{dt} = \frac{2\pi D_{gb}\delta_{gb}}{kTS}\left(p - p_{eq}\right) \tag{13}$$

where D_{gb} ($m^2 s^{-1}$) is the vacancy diffusion coefficient along grain boundaries, δ_{gb} (m) the thickness of the diffusion layer in grain boundaries, and the parameter S (-) depends on the fraction of grain faces covered by bubbles (fractional coverage) [29]. The the grain-boundary diffusion coefficient of vacancies is calculated using the expression [21, 29]

$$D_{gb} = 8.86 \times 10^{-6} \exp\left(-5.75 \times 10^{-19}/(kT)\right) \tag{14}$$

Grain-boundary bubble coalescence is also described, using the approach in [29, 30], which is based on a geometrical reasonig for the rate of bubble mechanical interaction during bubble growth.

FGR is modeled based on a principle of grain face saturation. More precisely, after the fractional coverage, F_c (-), attains a saturation value, $F_{c,sat}$, further bubble growth is compensated by gas release in order to maintain the constant coverage condition

$$\frac{dF_c}{dt} = \frac{d\left(N_{gf}A_{gf}\right)}{dt} = 0 \qquad \text{if } F_c = F_{c,sat} \tag{15}$$

This representation allows for the incubation behavior of thermal FGR [31]. Note that fission gas release and swelling are described as inherently coupled phenomena, as fission gas release from the grain faces counteracts bubble growth and thereby fission gas swelling.

2.4.2 Atomistic Model for Diffusivity

Atomistic calculations were recently performed at Los Alamos National Laboratory for the calculation of the diffusivity of gas atoms (Xe) in Cr_2O_3-doped UO_2. Through these calculations, new correlations for the parameter D that account for the specificities of Cr_2O_3-doped UO_2 relative to standard UO_2 were obtained. These correlations were implemented in the engineering model described above to produce a specific Cr_2O_3-doped UO_2 fission gas model. An account of the atomistic calculations is given hereinafter.

Out-of-pile experiments indicate that the diffusivity of fission gas is enhanced at high temperatures [32]. Killeen [33] also measured enhanced fission gas diffusivity, however only measurements at a single temperature were taken making extrapolation to the range of temperatures experienced by a fuel pellet impossible. Given this, atomic scale simulations are well poised to develop a Cr-doped UO_2 fission gas diffusivity model capable of describing in-pile behavior over a wide temperature range. The recent development at LANL of a comprehensive cluster dynamics (CD) model for fission gas diffusion in undoped UO_2 provides the ideal tool to investigate diffusion in doped UO_2 under irradiation conditions [34]. Modifications were made to this model on the basis that preferential reduction of Cr_2O_3 to Cr occurs

over the reduction of UO_{2+x} to perfectly stoichiometric UO_2, leading to the possibility of a two phase Cr-Cr_2O_3 regime as observed under certain conditions by Bourgeois et al. [35]. Therefore, the oxygen potential in the Cr-doped CD model can be defined based on the $Cr_2O_3 \leftrightarrow 2Cr + 3/2O_2$ equilibrium. To tackle known uncertainties within the underlying density functional theory (DFT) data small modifications were made to U, O, and electronic defect energies that ensured consistency with the thermodynamic data for $UO_{2\pm x}$ [36]. The oxygen potential in the undoped baseline case is not precisely known and will vary between experiments, but in this model it was selected to ensure a good agreement with the Turnbull fission gas diffusivity model [23, 24] used within Bison (Eq. 8). The results predict an enhanced diffusivity due to Cr doping for both the intrinsic and irradiation enhanced diffusion regimes. At temperatures below 1333 K the uranium vacancy concentration exceeds 1% and is beyond the validity of the point defect model used. Therefore, Arrhenius functions were fitted to the raw CD data to enable extrapolation to lower temperatures. These Arrhenius functions were reformulated to describe the enhancement in diffusivity with respect to the baseline undoped fission gas diffusivity (Eq. 8), as follows:

$$D^{doped} = \exp\left(-\frac{\Delta H_1}{k_B}\left[\frac{1}{T}-\frac{1}{T_1}\right]\right) D_1^{undoped} + \exp\left(-\frac{\Delta H_2}{k_B}\left[\frac{1}{T}-\frac{1}{T_2}\right]\right) D_2^{undoped} + D_3^{undoped} \tag{16}$$

where D is the diffusivity in m^2s^{-1}, $T_1 = T_2 = 1673$ K, $\Delta H_1 = 0.316$ eV, and $\Delta H_2 = -0.684$ eV. T and k_B are the temperature in K and Boltzmann constant in $eV{\cdot}K^{-1}$, respectively.

Equation 16 represents the case where the oxygen potential is entirely controlled by the $Cr_2O_3 \leftrightarrow 2Cr + 3/2O_2$ equilibrium and, as such represents the upper limit on enhancement of the fission gas atom diffusivity due to doping. On the other hand, under different conditions (e.g. significant excess oxygen in UO_{2+x}) the impact of doping could be negligible. The latter case would represent the case where another buffering mechanism is dominant for in-reactor conditions, such that the Cr_2O_3 reduction to Cr is insignificant.

2.4.3 Applicability and Uncertainty

The UO_2 fission gas model in Bison has been validated for normal LWR operating conditions, power ramps, and to a lesser extent, accidental conditions [21, 37–39].

Significant uncertainties exist in several parameters of the UO_2 fission gas model, which are discussed in [21]. In particular, following an extensive review of the available data, it was pointed out in [21] that the intra-granular diffusion coefficient of gas atoms, D, the re-solution rate, b, and the inter-granular diffusion coefficient of vacancies, D_{gb}, are each associated with an uncertainty as high as 2 orders of magnitude. As a result of the uncertainty analysis in [21], an uncertainty of a factor of 2–3 was associated with the calculated FGR. Additional discussion is provided in Section 5.1.

2.5 Gaseous Swelling (`UO2VolumetricSwellingEigenstrain`)

The total gaseous swelling is calculated on a physical basis, according to the evolution of inter-granular fission gas bubbles from the fission gas behavior model described in Section 2.4. The fuel fractional volumetric gaseous swelling is given by

$$\frac{\Delta V}{V} = \frac{1}{2}\frac{3}{r_{gr}} N_{gf} V_{gf} \tag{17}$$

where V (m^3) is the fuel volume, r_{gr} (m) the grain radius, $3/r_{gr}$ represents the grain surface to volume ratio, and the other variables are defined in Section 2.4.

2.6 Solid Swelling (`UO2VolumetricSwellingEigenstrain`)

2.6.1 Model Choice

While fuel gaseous swelling in Bison is calculated using the coupled FGR-gaseous swelling model described in Section 2.4, for swelling due to solid fission products an empirical relation from MATPRO [16] is used. Solid fission

product swelling is expressed as a simple linear function of burnup:

$$\Delta\epsilon = 5.577 \times 10^{-5} \rho \Delta bu \tag{18}$$

where $\Delta\epsilon$ (/) is the volumetric solid swelling increment, Δbu (fissions/atoms- U) the burnup increment, and ρ is the fuel density (kg/m^3).

2.6.2 Applicability and Uncertainty

Following [1], the MATPRO solid swelling correlation used in Bison is considered to be applicable to fuels with burnups up to 100 GWd/tU.

As for the uncertainty associated with the solid swelling model, an uncertainty range (95% confidence interval of a Gaussian distribution) of ±20% is considered, in line with [10]. This is also compatible with the uncertainty estimated in [1].

2.7 Densification (`UO2VolumetricSwellingEigenstrain`)

2.7.1 Model Choice

Densification of UO_2 in Bison is computed using a modified version of the ESCORE model described in [40]. Typically, the total fuel densification saturates at a value of the order of 1% volumetric deformation for UO_2. A value of 1% for the maximum fuel densification is used in the Bison model. Some experiments have shown, however, that doping with Cr_2O_3 has resulted in a lower fuel densification compared to pure UO_2. Fuel densification was evaluated in the Halden experiment IFA-677.1 for both Cr_2O_3-doped UO_2 and pure UO_2 fuel rods irradiated under HBWR (Halden Boiling Water Reactor) conditions at average linear heat rates in the range ∼30-45 kW/m [41]. The observed maximum fuel densification was ∼0.60% for standard UO_2 fuel and ∼0.10% for chromium-doped UO_2 [41]. Fuel densification was also evaluated in the Halden experiment IFA-716.1 for both Cr_2O_3-doped UO_2 and pure UO_2 fuel rods irradiated under HBWR conditions at average linear heat rates of ∼24-30 kW/m [6, 42]. Densification was very low or negligible for the chromium-doped UO_2 rods, while a maximum densification of ∼0.3% was observed for the standard UO_2 rod.

In the absence of a specific densification model for Cr_2O_3-doped UO_2, in Bison the same model used for pure UO_2 is adopted at this time. However, to account for the low densification in Cr_2O_3-doped UO_2 observed in the Halden experiments, the total fuel densification in Bison is set to a lower value (0.1%) relative to the default value used for pure UO_2, following the experimental information currently available.

2.7.2 Applicability and Uncertainty

The current approach to model fuel densification in Bison is expected to be applicable to fuels with characteristics similar to the fuel rods in the IFA-677.1 and IFA-716.1 experiments [6, 42–45]. Further experimental investigation is necessary before more general and definitive conclusions on the suppression of fuel densification as a result of Cr_2O_3 doping.

Considering the information discussed above, in this work an uncertainty in the maximum fuel densification in Cr_2O_3-doped UO_2 ranging from a value of zero (i.e., densification is neglected) to the value of 1% volumetric deformation used for pure UO_2 is considered. This range is intended to account for the possibility of complete suppression of densification (based on the Halden observations) as a lower bound, and a behavior analogous to undoped fuel as an upper bound for the amount of densification.

2.8 Elasticity and Cracking (`UO2IsotropicDamageElasticityTensor`)

The `UO2IsotropicDamageElasticityTensor` model in Bison computes the elasticity tensor of UO_2 from the Young's modulus and Poisson's ratio. In this model, the effect of fuel cracking is represented in a simple way through a scaling

of the Young's modulus and Poisson's ratio as a function of the number of cracks present in the fuel. Cr_2O_3 doping is not expected to have a significant effect on the elastic behavior of uncracked fuel. Accordingly, we calculated the elastic constants for uncracked fuel using correlations for standard UO_2. In particular, the MATPRO models `FELMOD` and `FPOIR` are applied for the Young's modulus and Poisson's ratio, respectively [16]. The corresponding correlations are

$$E = 2.334 \times 10^{11} \left(1 - 1.0915 \times 10^{-4}\, T\right) (1 - 2.752\, P) \tag{19}$$

where E (Pa) is the Young's modulus, T (K) the temperature, and P (/) the fuel porosity, and

$$\nu = 0.316 \tag{20}$$

where ν (/) the Poisson's ratio.

Concerning the cracking behavior of Cr_2O_3-doped UO_2 fuel pellets relative to standard UO_2, larger grain sizes can reduce the fracture strength of brittle materials. As reviewed in [3], work on undoped UO_2 found that the fracture stress is lower in 25 μm grains compared to 8 μm grains [46]. Given the larger grains for doped UO_2 it can be expected that the fracture strength will be further reduced. Oguma [47] showed that increasing porosity, grain size, and pore size all result in reduced fracture strength. Dopant inclusions within the pellets might further alter the fracture strength by weakening grain boundaries or by introducing stress raisers. However, it is stated in [7] that experimental work at AREVA on Cr_2O_3-doped UO_2 is consistent with the work of Oguma. It is also discussed that the reduced fracture strength is responsible for a larger number of small cracks in the periphery of the pellet and that this is beneficial for PCI performance.

In the absence of more conclusive information and of a specific fuel cracking model for Cr_2O_3-doped UO_2, in this work the effect of cracking on the fuel mechanical behavior is accounted for in Bison using a relatively simple model for UO_2. The model describes the cracked material as an isotropic material with scaled elastic constants (isotropic softening model). The formulas for the elastic constants of the cracked fuel are

$$E_{cracked}(n) = [f(\nu)]^n E \tag{21}$$

$$\nu_{cracked}(n) = \frac{\nu}{2^n + (2^n - 1)\nu} \tag{22}$$

where n (-) is the number of cracks, and E, ν are calculated using Eqs 19 and 20. The number of cracks is estimated using an empirical relation as a function of the rod average linear heat rate. Derivation and details for this model are given in [48].

2.8.1 Applicability and Uncertainty

The correlation for the Young's modulus, Eq. 19, is applicable up to the melting temperature of UO_2 (~3113 K). However, as no data are available above 1500K, the correlation was extrapolated to the higher temperatures [16]. The best estimate for the standard error associated with this model is the standard deviation of Eq. 19. The value, 0.06×10^{11} N/m^2, or about 3% of the predicted value, includes the effect of sample to sample variation but does not include the artificial error due to the extrapolation of the temperature coefficient [16]. For temperatures above 1600 K, there are no data and no rigorous ways to test the model. In Eq. 19, the standard error estimate has been increased by an additive term, which is zero at 1600 K and increases to 0.25% of the predicted value at the approximate melting temperature (3113 K) [16].

For the Poisson's ratio of UO_2, in addition to the value of 0.316 in Eq. 20, values of 0.314 and 0.306 have been reported, as reviewed in [16]. On this basis, the uncertainty in the Poisson's ratio is preliminarily estimated as ~0.01, or ~3%.

2.9 Creep (`UO2CreepUpdate`)

Cr_2O_3-doped UO_2 may be less prone to PCI failures during ramp tests thanks to a larger creep rate compared to standard fuel [49]. However, more specific information and creep models for Cr_2O_3-doped UO_2 are still not available. Hence,

while creep modeling developments specific to doped fuel are left to future efforts, in the present work the fuel creep model for standard UO_2 is applied in the Bison simulations. The constitutive relation is taken from the MATPRO `FCREEP` model [16]. The creep rate depends on the Von Mises stress, temperature, fission rate, fuel density, grain radius, and O/M ratio. Hence, even if the model is not specific to doped fuel, the effect of a larger grain radius in Cr_2O_3-doped UO_2 relative to standard UO_2 is considered in the creep rate through the grain radius dependence.

3 Uranium Silicide (U_3Si_2)

U_3Si_2 fuel is a potentially attractive alternative to the traditional UO_2 fuel currently used in LWRs because of its higher thermal conductivity and uranium density. Material models for U_3Si_2 available in the Bison fuel performance code are described in the following subsections including a description of how the correlation or model was developed, the applicability of the model, and its associated uncertainty. In some cases, the uncertainty in the model varies over the range of applicability (e.g., the uncertainty is higher at larger temperatures). In other cases, a conservative approximation is assumed in the absence of any other information. If the model is empirical in nature the uncertainty is derived from the experimental data upon which the model was created and in the case of multiscale developed models the uncertainty in the lower length scale calculations and parameters are propagated to the engineering scale. The name of the C++ class that computes the respective properties within Bison is listed in parentheses in the subsection header. The details described below can also be found in the online theory and user documentation packaged with the Bison code.

3.1 Thermal Properties (`ThermalSilicideFuel`)

The `ThermalSilicideFuel` model in Bison computes the thermal conductivity and specific heat of U_3Si_2 as a function of temperature. The model contains multiple options for both thermal conductivity (`WHITE`, `SHIMIZU`, `ZHANG`, `ARGONNE`, `HANDBOOK`) and specific heat (`WHITE`, `IAEA`, `HANDBOOK`).

3.1.1 Model Development

Thermal Conductivity Models

The (`WHITE`) thermal conductivity model is given by the corrigendum [50] to [51] and is based upon thermal diffusivity calculations

$$k = 4.996 + 0.0118T \tag{23}$$

where T is temperature in K and k is the thermal conductivity in W/m-K. An alternative model (`SHIMIZU`) is available and based upon the experimental data for induction cast U_3Si_2 fuel pellets in the radial direction from [52]

$$k = 7.98 + 0.0051(T - 273.15) \tag{24}$$

where T is temperature in K. According to [53] this expression may underestimate the true thermal conductivity of U_3Si_2. A third option (`ZHANG`) is more sophisticated because it is able to determine the thermal conductivity of pure uranium metal, pure silicon, U_3Si_2, U_3Si_5, and U_3Si. By utilizing details from [54–56], Zhang arrived at an equation of the form

$$k(c) = \frac{(1-c)/w_e^U + c/w_e^{Si}}{1 + c(1-c)\left(L_1 + L_2\left(c^2 - (1-c)^2\right)\right)} \tag{25}$$

where c is the silicon concentration (given as mole fraction in the fuel). For example, for U_3Si_2 c=0.4. $1/w_e^U$ and $1/w_e^{Si}$ are the conductivities of U and Si, respectively. L_1 and L_2 are fitting parameters. The first step is to find the values of w_e^U and w_e^{Si}. It was found that an exponential decay function can be used to reproduce these values

$$w_e = m_0 + m_1 e^{(-\frac{T-T_0}{T_1})} + m_2 e^{(-\frac{T-T_0}{T_2})} \tag{26}$$

where T is the temperature in K and, m_0, m_1, m_2, T_0, T_1, and T_2 are parameters unique to U or Si. The values of these parameters are summarized in Table 2.

Zhang then used the data from [51] for U_3Si_2 and [57] for U_3Si_5 to fit the parameters L_1 and L_2. The equation for these parameters are 5th order polynomials of temperature given by

$$L_1 = 6.0959 - 0.01457T + 1.75527 \times 10^{-5}T^2 - 1.13428 \times 10^{-8}T^3 + 4.05139 \times 10^{-12}T^4 - 6.04924 \times 10^{-16}T^5 \tag{27}$$

Table 2: Parameters used to fit the intrinsic thermal resistivity of U and Si

Parameters	m_0	m_1	m_2	T_0	T_1	T_2
U	0.00448	0.0089	0.03267	0.0	500.76917	1555.4716
Si	0.08303	29.152	3.88841	645	87.48315	252.19318

$$L_2 = -1.82488 + 0.0148T - 2.92953 \times 10^{-5}T^2 + 2.68933 \times 10^{-8}T^3 - 1.15846 \times 10^{-11}T^4 + 1.90712 \times 10^{-15}T^5 \quad (28)$$

It is cautioned that the 5th order polynomial for L_1 is based upon the data of [51] prior to the corrigendum [50] which corrected the thermal diffusivity calculation. The final option for thermal conductivity of U_3Si_2 is given by a correlation from the U_3Si_2 handbook. [58]. The correlation is a polynomial fit to the data of [50, 52, 59, 60]

$$k = 9.029 \times 10^{-15}T^5 - 4.609 \times 10^{-11}T^4 + 8.676 \times 10^{-8}T^3 - 7.485 \times 10^{-5}T^2 + 4.166 \times 10^{-2}T + 0.5211 \quad (29)$$

where T is temperature in K.

All of the preceding models are for unirradiated thermal conductivity only. Miao et al. [61] utilized rate theory calculations to develop a model that can predict the degradation of thermal conductivity due to both intergranular and intragranular bubbles. Based upon the rate theory results tricubic interpolation is used to calculate temperature, temperature gradient, and fission density (burnup) dependent degradation factors applied to the intrinsic thermal conductivity which can be calculated from any of the unirradiated thermal conductivity models (`WHITE`, `SHIMIZU`, `ZHANG`, or `HANDBOOK`). The intrinsic thermal conductivity is calculated as follows

$$k_{in} = \frac{k_{unirr}}{1 - k_{unirr}\frac{R}{g}} \quad (30)$$

where k_{unirr} is the unirradiated thermal conductivity from one of the previously described models, R is the Kapitza resistance (2.5e-8 m^2-K/W), and g is the grain size (taken as 35 μm). The modified Kapitza resistance is determined based upon the amount of grain boundary coverage

$$GB_{cov} = FCOV/3000.0 \quad (31)$$

where GB_{cov} is the grain boundary coverage, and $FCOV$ is obtained from the tricubic interpolation of the data tables generated by the rate theory calculations. The modified Kapitza resistance is then determined by

$$R' = R\left(1 - GB_{cov}\right)^{0.86+0.3ln(R)} \quad (32)$$

The first degradation factor known as the intergranular factor is then computed by

$$f_{inter} = \frac{1.0}{1.0 - k_{in}\frac{R'}{g_g}} \quad (33)$$

where g_g is the grain size specified in the GRASS-SST rate theory calculation (5.0 μm) The second degradation factor known as the intragranular factor is calculated by

$$f_{intra} = \frac{1.0 - GSWb}{1.0 + 0.9GSWb} \quad (34)$$

where $GSWb$ is the intragranular gaseous swelling strain due to intragranular bubbles is obtained from the tricubic interpolation of the data tables generated by the rate theory calculations. Finally the thermal conductivity is then given as

$$k = k_{in}f_{inter}f_{intra} \quad (35)$$

Specific Heat Models

The WHITE model for the specific heat capacity U_3Si_2 is fit to the data [51]

$$C_p = 140.5 + 0.02582T \tag{36}$$

where T is temperature in K and C_p is the specific heat capacity is in J/mol-K. The calculated value for C_p needs to be divided by the molar mass of U_3Si_2 taken as 0.77025773 kg/mol. An alternative correlation from[62] (IAEA) is based upon research reactor data and is given by:

$$C_p = 199 + 0.104(T - 273.15) \tag{37}$$

where T is temperature in K. The first version of the U_3Si_2 handbook [63] provided the following correlation for specific heat:

$$C_p = 1000.0\left(3.52 \times 10^{-5}T + 0.18\right) \tag{38}$$

where T is temperature in K and C_p is the specific heat capacity is in J/kg-K. The updated version of the U_3Si_2 handbook [63] suggests the correlation given by the WHITE model. If one examines the correlations of the WHITE and HANDBOOK models it is observed that they are in fact equivalent once the value of C_p is output in J/kg-K.

3.1.2 Applicability and Uncertainty

Both the WHITE thermal conductivity and specific heat models are valid from room temperature to 1773 K. The SHIMIZU thermal conductivity model is valid from 473 K to ∼1273.15 K. Since the ZHANG model uses data from [51, 57] it is assumed that the range of applicability is the same as the WHITE model. The HANDBOOK thermal conductivity model incorporates recent low temperature measurements and is therefore valid from 13 K to 1500 K. For the HANDBOOK specific heat model the temperature range is reduced to be between 293 K and 1500 K. The range of applicability of the IAEA specific heat model is not provided by [62] but can be obtained from the original data [52] upon which the correlation was developed. The temperature range of applicability of the IAEA model is between 323 K to 973 K. The rate theory thermal conductivity degradation model is a function of temperature (T), temperature gradient (G), and fission density (f). The range of applicability of these three parameters are given by

$390 \leq T \leq 1190$ K

$0 \leq G \leq 160$ K/mm

$0 \leq f \leq 2.5755 \times 10^{21}$ fissions/cm^3

White et al. [51] state that the correlation for the WHITE specific heat model is within ± 3% of the experimental values for all temperatures. Therefore, the uncertainty in the WHITE specific heat model is taken as ±3%. Since the HANDBOOK specific heat model is equivalent its uncertainty is also taken as ±3%. By propagating the uncertainty in the their specific heat model, density calculations, and thermal diffusivity calculations White et al. [51] obtained the uncertainty in the WHITE thermal conductivity model, which is ±5%. The uncertainty of the IAEA model is not provided and cannot be calculated from the data given in either [52] or [62]. The SHIMIZU thermal conductivity model has a maximum deviation from the experimental data upon which it is based by approximately 4%. Therefore, the uncertainty on the model is taken as ±4% (See Figure 2).

The HANDBOOK model incorporates both new and old experimental data in its formulation. Recall that induction cast data used for the SHIMIZU model was identified to likely underpredict the true thermal conductivity of the U_3Si_2 and therefore is not included in the HANDBOOK polynomial fit. In addition, the induction case data is not used in determining the uncertainty range. The experimental data point with the largest deviation from the polynomial fit line corresponds to the arc-cast data point at a temperature of ∼1110 K with a thermal conductivity value of ∼22.47 W/m-K. This calculation results in a 95% confidence band of ±18.2%. Figure 3 reproduces a similar plot to the U_3Si_2 handbook with the added dashed lines for the uncertainty assumed in the Bison model.

Finally, the uncertainty in the tricubic interpolation thermal conductivity degradation model is unknown as [61] did not provide uncertainties in the parameters used in the rate theory calculations that could be propagated into the degradation

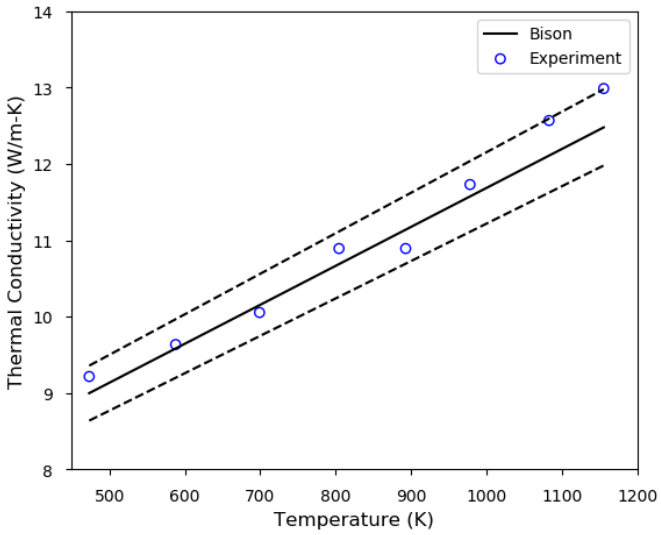

Figure 2: Shimizu thermal conductivity model with associated uncertainty provided by the dashed lines. Adapted from [52].

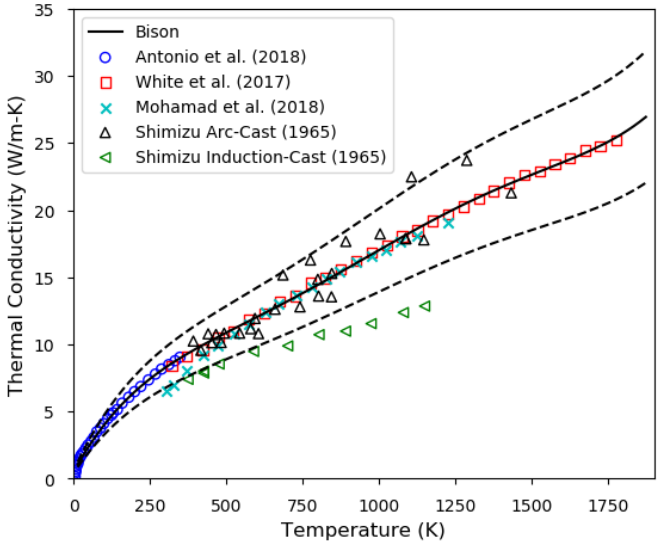

Figure 3: Handbook model with associated uncertainty provided by the dashed lines. Adapted from [58].

factors. However, these degradation factors assume constant values for many of the parameters, including the Kaptiza resistance, grain size, and grain size specified in the GRASS-SST rate theory calculations. It is known that these values should vary and have an associated uncertainty. In absence of additional information, a conservative approach of assigning a 10% uncertainty to each of the degradation factors (intergranular and intragranular) is adopted.

3.1.3 Model Recommendations

Numerous models have been presented for the thermal properties of U_3Si_2 based upon variety of experimental data obtained over multiple decades. The earlier measurements were primarily for U_3Si_2 fabricated for research reactor applications while the later measurements were for LWR applications. Thus, it is recommended that the `HANDBOOK` model be used for the unirradiated thermal conductivity of U_3Si_2 as it incorporates both older and new data in its formulation. If thermal conductivity degradation is desired, the degradation model may be applied. For consistency,

the HANDBOOK model for specific heat is suggested.

3.2 Elasticity (U3Si2ElasticityTensor)

The U3Si2ElasticityTensor model in Bison computes the elasticity tensor of U_3Si_2 from the Young's modulus and Poisson's ratio as a function of porosity.

3.2.1 Model Development

The model is empirical in nature and was obtained from the U_3Si_2 handbook [58]. A linear fit to the data set provided by [64] is provided in the handbook. Given the limited amount experimental data, it was decided for the Bison model to incorporate all the experimental data available including Carvajal-Nunez et al. [65] and Mohamad et al. [59]. The linear fits are illustrated along with the experimental data for Young's modulus (black) and shear modulus (blue) in Figure 4. To avoid cluttering the figure, equations of the linear fits are provided below. The equation for Young's modulus is given by

$$E = -6.425p + 142.68 \tag{39}$$

where E is the Young's modulus (GPa) and p is the porosity (%). The shear modulus is given by

$$G = -2.901p + 61.27 \tag{40}$$

where G is the shear modulus (GPa) and p is the porosity. Once E and G are known Poisson's ratio can be calculated from

$$\nu = \frac{E}{2.0G} - 1.0 \tag{41}$$

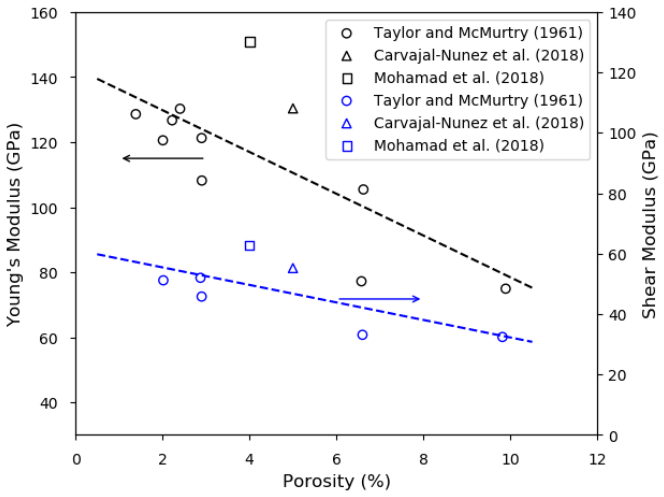

Figure 4: Young's and shear modulus data with trendline. Adapted from the U_3Si_2 Handbook [58].

The porosity in percent is calculated from the current density through

$$p = \left(1.0 - \frac{\rho_{current}}{\rho_{theoretical}}\right) \times 100\% \tag{42}$$

where $\rho_{current}$ and $\rho_{theoretical}$ are the current and theoretical densities of U_3Si_2 respectively. The theoretical density is taken as 12200 kg/m^3.

3.2.2 Applicability and Uncertainty

The correlations for Young's modulus and shear modulus are valid over a porosity range of 1.5 to 10%.

Given the limited amount of data for the elastic properties of U_3Si_2 the suggested model is designed to capture all of the data points in Figure 4 within 95% confidence assuming a normal (Gaussian) distribution. Thus, the calculated uncertainty corresponds to two standard deviations about the mean given by the correlations in Equations 39 and 40. The data points for Young's (~151 GPa) and shear (~63 GPa) modulus from Mohamad et al. [59] are used to determine the bounds of the model given that it represents the furthest known value from the best fit correlations. The calculated uncertainty is 29.1% and 26.8% for Young's modulus and shear modulus, respectively. Figure 5 illustrates the correlation with the assumed uncertainty over the porosity range over which the model is applicable. Dashed black and blue lines correspond to the uncertainty bands on Young's modulus and shear modulus, respectively.

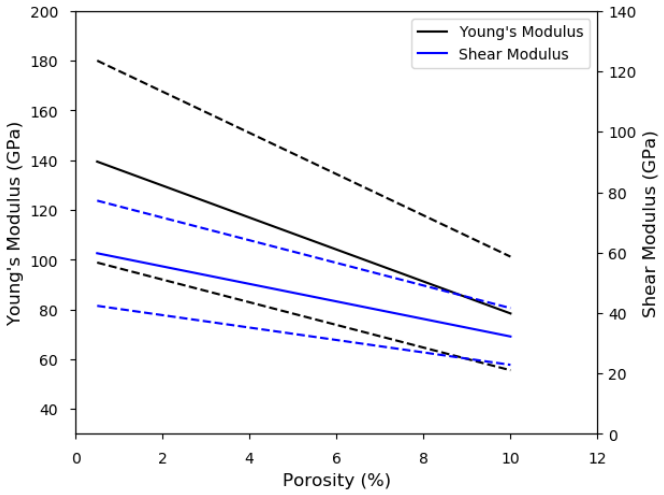

Figure 5: Young's and shear modulus correlations with their associated uncertainty bands.

3.3 Thermal and Irradiation Creep (`U3Si2CreepUpdate`)

The `U3Si2CreepUpdate` model in Bison computes the thermal and irradiation creep rate and strain for U_3Si_2 as a function of temperature and applied stress. Two models are available in Bison to predict the creep behavior of U_3Si_2, `FREEMAN` and `METZGER`.

3.3.1 Model Development

The `FREEMAN` model captures only secondary thermal creep of U_3Si_2 through an Arrhenius law based upon compressive creep experiments completed at the University of South Carolina. Details of the derivation of the pre-exponential constant, stress exponent, and activation energy can be found in [66]. The creep rate is given by

$$\dot{\epsilon} = 2.0386 \times 10^{-4} \sigma^{1.2063} \exp\left(\frac{295550}{RT}\right) \tag{43}$$

where R is the ideal gas constant (8.314 J/mol-K) and T is the temperature in K.

The `METZGER` model is derived from first principles including knowledge of uranium carbide for which [67] assumes the creep behavior of U_3Si_2 will be similar. The model accounts for irradiation induced creep below a homologous temperature of 0.45 T_m (872.0 K) through a Nabarro-Herring mechanism

$$\dot{\epsilon}_{NH} = \frac{A_{NH} D_{irr} b^3 \sigma}{kTd^2} \tag{44}$$

where A_{NH} is Nabarro-Herring creep coefficient, D_{irr} is the diffusion coefficient under athermal conditions, b is the burgers vector, σ is the Von Mises stress in Pa, k is the Boltzmann constant, T is the temperature in K, and d is the grain size. Above a homologous temperature of 0.45 T_m the creep can either driven by a Coble grain boundary creep mechanism or a dislocation creep mechanism depending upon the stress state derived from a generalized Ashby diagram. If $\sigma/G > 10^{-4}$ where G is the shear modulus of U_3Si_2, which is assumed to be constant at 50 GPa in this model, then the creep mechanism is governed by dislocations through

$$\dot{\epsilon}_{dis} = \frac{A_{dis} D_L b \sigma^5}{kTG^4} \tag{45}$$

where A_{dis} is the dislocation creep coefficient, and D_L is the lattice diffusion coefficient. if $\sigma/G \leq 10^{-4}$ then creep occurs due to a Coble grain boundary mechanism given by

$$\dot{\epsilon}_{co} = \frac{A_{co} D_{gb} b^4 \sigma}{kTd^3} \tag{46}$$

where A_{co} is the Coble creep coefficient, and D_{gb} is the grain boundary coefficient. The diffusion coefficients in the three different regimes are given by

$$D_{irr} = D_{o_{gb}} \exp\left(-\frac{Q_{gb}}{872.0k}\right) \tag{47}$$

$$D_{gb} = D_{o_{gb}} \exp\left(-\frac{Q_{gb}}{kT}\right) \tag{48}$$

$$D_L = D_{o_L} \exp\left(-\frac{Q_L}{kT}\right) \tag{49}$$

where $D_{o_{gb}}$ and D_{o_L} are coefficients, and Q_{gb} and Q_L are activation energies. The values assumed by the model for all the parameters are summarized in Table 3. The leading coefficients in the diffusion coefficient laws are obtained from sintering models.

Table 3: Values for different parameters used in the Metzger creep model

Parameters	Value	Units
A_{NH}	12.5	(-)
A_{dis}	6×10^{7}	(-)
A_{co}	40.0	(-)
$D_{o_{gb}}$	2365.0	m^2/s
D_{o_L}	6.86×10^{24}	m^2/s
Q_{gb}	9.97×10^{-19}	J
Q_L	2.0×10^{-18}	J
b	0.56×10^{-9}	m
k	1.38064852×10^{-23}	J/K
d	20×10^{-6}	m

3.3.2 Applicability and Uncertainty

The `FREEMAN` model is based upon limited compressive creep experiments. The ranges of applied stress and temperature of these experiments varied between ~44.0 to ~80 MPa and ~1125 to ~1225 K. Therefore, the model which is developed based upon these experiments is assumed to have a range of applicability within these experimental conditions. This limits the usefulness of the model to a relatively narrow band. On the other hand the `METZGER` model was developed from a first principles perspective and is applicable from room temperature up to the melting temperature of U_3Si_2 (~1938 K).

Determination of the uncertainty in creep rate predictions by the FREEMAN model is relatively straightforward. Freeman et al. [66] created a plot illustrating the calculated creep rate as a function of the experimental creep rate. A modified version of that plot is shown in Figure 6. The solid 1:1 line corresponds to a perfect prediction of the experiments by the model. Points above the line represent predicted creep rates greater than the experimental measurements and points below the line represent underprediction of the creep rate. For conservatism, the data point furthest from the 1:1 line is taken as the 95% confidence interval (two standard deviations) about the mean value produced by the correlation. The uncertainty determined from the data point at (meas. $= 0.469\times10^{-7}s^{-1}$, calc. $= 0.856\times10^{-7}s^{-1}$) is a factor of 1.83. Thus, dashed lines representing $\pm$ a factor of 1.83 are included in Figure 6.

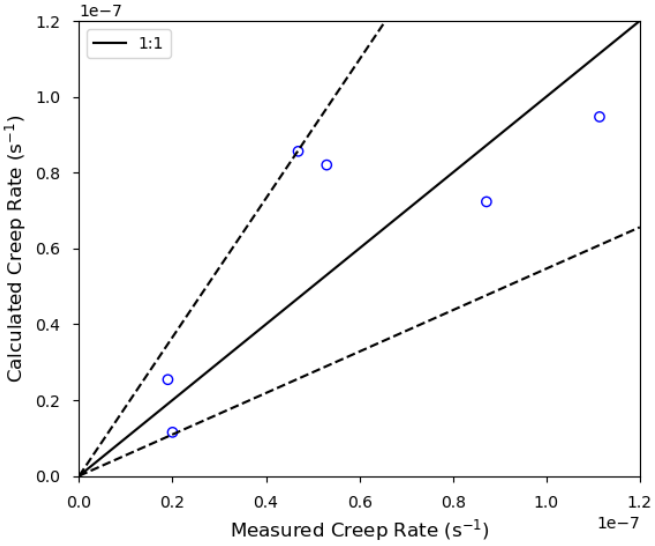

Figure 6: Calculated versus measured creep rates. A region of $\pm$ a factor of 1.83 shown around the 1:1 line.

The uncertainty in the METZGER model cannot currently be quantified from the first principles derivation. All of the constants and other parameters are derived from the slope of a single plot of grain growth data. Performing uncertainty on the grain growth data only changes the y-intercept of the fit and not the slope itself. Current lower length scale work is being completed to improve the diffusion coefficients used by the METZGER model. Once complete the uncertainty in the diffusion coefficients from the lower length scale calculations can be propagated into the prediction of the creep rate. In the mean time, a conservative assumption similar to that of the FREEMAN model (a factor of $\sim$1.83) is recommended.

3.3.3 Model Recommendation

Due to its larger ranges of applicability in temperature and applied stress the METZGER model is recommended. This model also allows for improvements through direct input of the results from lower length scale density functional theory (DFT) calculations the future.

3.4 Thermal Expansion (U3Si2ThermalExpansionEigenstrain)

The U3Si2VolumetricSwellingEigenstrain model in Bison computes the thermal expansion coefficient and thermal strain of U_3Si_2 as a function of temperature.

3.4.1 Model Development

The correlation for thermal expansion from the first release of the U_3Si_2 handbook [63] describes the instantaneous linear thermal expansion coefficient (K^{-1}) as a function of temperature based upon the data of [64]

$$\alpha = 1.42 \times 10^{-9} T + 1.30 \times 10^{-5} \tag{50}$$

where the temperature (T) is in K. An incremental approach using the average coefficient of thermal expansion over the time step given the incremental temperature change is used for computing the thermal strain

$$\epsilon_{thermal}^{current} = \epsilon_{thermal}^{old} + \left(T_{current} - T_{old}\right) \frac{\alpha_{current} + \alpha_{old}}{2.0} \tag{51}$$

where *current* refers to the current time step and *old* refers to the previous time step. Another alternative is to specify a constant temperature independent thermal expansion coefficient.

3.4.2 Applicability and Uncertainty

The correlation for the instantaneous linear thermal expansion model for U_3Si_2 is valid in the temperature range of 273 K to 1473 K. The thermal expansion correlation provided by Equation 50 is on the lower end of the available experimental data provided in the latest release of the U_3Si_2 handbook [58]. However, the scatter in data is quite large (See Figure 7. To encompass all of the data [51, 52, 59, 64, 68] including the best fit equation currently in Bison, it would be sufficient to simply supply a constant instantaneous linear thermal expansion coefficient as a function of temperature with associated uncertainty. The suggested value is $(16.0 \pm 3.0) \times 10^{-6} K^{-1}$.

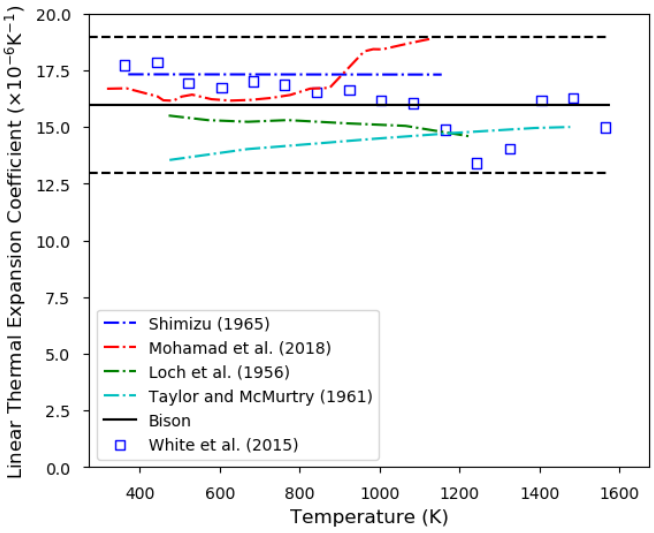

Figure 7: Thermal expansion data with the suggested constant value and uncertainty bands included. Based upon a Figure from the U_3Si_2 handbook [58].

3.5 Fission Gas Behavior (`U3Si2FissionGas`)

The Bison model for fission gas behavior in U_3Si_2 incorporates the fundamental physical mechanisms of fission gas behavior and calculates the coupled fission gas release (FGR) and gaseous swelling concurrently. Given the lack of experimental data for U_3Si_2 under LWR conditions, a multiscale approach has been adopted for model development, where the engineering Bison model is informed with parameters calculated via atomistic and meso-scale simulations. Considering that U_3Si_2 under LWR conditions retains a polycrystalline structure, fission gas behavior is modeled as

consisting of two main stages, i.e., intra-granular and inter-granular behavior, by analogy with UO_2. Correspondingly, the model includes components for intra-granular and inter-granular behavior of fission gases. The intra-granular component is based on cluster dynamics and computes the evolution of intra-granular fission gas bubbles and swelling coupled to gas diffusion to grain boundaries. The inter-granular component describes the evolution of grain-boundary fission gas bubbles coupled to fission gas release. The current Bison model is based on the development described in [69]. However, improvements have been made in the present version which are based on recent lower length-scale calculations. These include, in particular, atomistic calculations to better assess the diffusion coefficients of fission gas atoms and vacancies in U_3Si_2, which were performed at Los Alamos National Laboratory. The latest model, applied in the present work, also includes improved parameters based on molecular dynamics calculations in [70].

The engineering model is described in Section 3.5.1, and the atomistic calculations for diffusivity are described in Section 3.5.2. Some more details are given in Section 5.2, where a sensitivity analysis for U_3Si_2 modeling is discussed.

3.5.1 Engineering Model Development

Intra-granular Model

The intra-granular component of the model provides calculation of the gas diffusion rate to grain boundaries and of the intra-granular fission gas bubble swelling, based on a description of intra-granular bubble evolution in terms of number density and average size.

The equations governing the evolution of number density and gas atom content of intra-granular bubbles, and the coupled diffusion of single gas atoms to grain boundaries, are:

$$\begin{aligned}
\frac{dN_{ig}}{dt} &= \nu - b' N_{ig} \\
\frac{\partial c}{\partial t} &= D\nabla^2 c - gc + bm - 2\nu + \beta \\
\frac{\partial m}{\partial t} &= +gc - bm + 2\nu
\end{aligned} \tag{52}$$

where N_{ig} (m^{-3}) is the number density of intra-granular bubbles, c and m (m^{-3}) the intra-granular gas concentration in the matrix and in the bubbles, respectively, t (s) the time, D ($m^2 s^{-1}$) the diffusion coefficient of single gas atoms, r (m) the radial coordinate in the spherical grain, β ($m^{-3} s^{-1}$) the gas generation rate, g (s^{-1}) the trapping rate, and b (s^{-1}) the re-solution rate. $b' = b/(n_{a,ig} - 1)$, with $n_{a,ig} = m/N$ being the average number of gas atoms per bubble, accounts for the fact that a bubble containing n gas atoms will require on average $n-1$ homogeneous re-solution events before being destroyed. A detailed derivation is provided in [69].

The set of coupled partial differential equations in Eq. 52, is solved using the recently developed PolyPole-2 algorithm [71], extended to the solution of the 3-equation system. Details of this extension are not given here for brevity, however, the concept of the algorithm is the same as described in [71].

Intra-granular bubble growth is computed based on the evolution of the gas atom content from Eq. 52 and the rate of absorption of vacancies at the bubble. The bubble growth/shrinkage rate is calculated as

$$\frac{\mathrm{d}V_{ig}}{\mathrm{d}t} = \omega \frac{\mathrm{d}n_{a,ig}}{\mathrm{d}t} + \Omega \frac{\mathrm{d}n_{v,ig}}{\mathrm{d}t} \tag{53}$$

where ω (m^3) is the van der Waals atomic volume for xenon, $n_{v,ig}$ the number of vacancies per intra-granular bubble, and Ω (m^3) the vacancy volume. In general, bubbles are in a non-equilibrium state and tend to the equilibrium condition by absorbing or emitting vacancies. The vacancy absorption/emission rate can be calculated based on the approach in [28] as

$$\frac{\mathrm{d}n_{v,ig}}{\mathrm{d}t} = \frac{2\pi D_{ig}^{v} \rho}{kT\zeta}(p_{ig} - p_{ig,eq}) \tag{54}$$

where D_{ig}^{v} ($m^2\ s^{-1}$) is the intra-granular vacancy diffusion coefficient, ρ (m) the radius of the equivalent Wigner-Seitz cell surrounding a bubble and influenced by the vacancy absorption/emission, k ($J\ K^{-1}$) is the Boltzmann constant, T (K) is the local temperature, and ζ (dimensionless) is a geometric parameter that is calculated as [69]

$$\zeta = \frac{10\psi(1+\psi^3)}{-\psi^6+5\psi^2-9\psi+5} \tag{55}$$

where $\psi = R_{ig}/\rho$. The present model for vacancy absorption/emission at intra-granular bubbles is a reformulation of the Speight and Beere model for behavior at grain boundaries of bubbles of circular projection (2D problem) [28]. In particular, Eqs. 54, 55 represent the equivalent model for vacancy absorption/emission at spherical bubbles in the bulk (3D problem). The mechanical equilibrium of an intra-granular bubble, assumed to be spherical, is governed by the Young-Laplace equation

$$p_{ig,eq} = \frac{2\gamma}{R_{ig}} - \sigma_h \tag{56}$$

where γ ($J\ m^{-2}$) is the U_3Si_2/gas surface energy, R_{ig} the intra-granular bubble radius, and σ_h (Pa) is the hydrostatic stress. The pressure of the gas in the bubble, p_{ig} (Pa), is calculated based on the van der Waals equation of state.

Finally, the fractional volumetric intra-granular fission gas swelling is given by

$$\left(\frac{\Delta V}{V}\right)_{ig} = V_{ig} N_{ig} \tag{57}$$

Inter-granular Model

The numerical solution of Eq. 52 allows for the calculation of the arrival rate of gas at the grain boundaries, providing the source term for the inter-granular gas behavior module. This computes both grain-boundary fission gas swelling and fission gas release through a direct description of the grain-boundary bubble development. The concept of the inter-granular model is the same as the UO_2 model developed in [21, 30], see also Section 2.4. However, the material parameters are specific to U_3Si_2 and were calculated via lower length-scale modeling. The main assumptions and characteristics of the model are as follows.

The absorption rate of gas at the inter-granular bubbles is assumed to equal the arrival rate of gas at the grain boundaries. An initial number density of inter-granular bubbles, $N_{gb,0}$, is considered, and further nucleation during the irradiation is neglected (one-off nucleation). All grain-boundary bubbles are considered to have, at any instant, equal size and equal lenticular shape of circular projection. Grain-boundary bubble growth (or shrinkage) by inflow of gas atoms from within the grains and concomitant absorption (or emission) of vacancies from the grain boundaries is considered. The inter-granular bubble growth/shrinkage rate is calculated as

$$\frac{\mathrm{d}V_{gb}}{\mathrm{d}t} = \omega\frac{\mathrm{d}n_{a,gb}}{\mathrm{d}t} + \Omega\frac{\mathrm{d}n_{v,gb}}{\mathrm{d}t} \tag{58}$$

where V_{gb} (m^3) is the inter-granular bubble volume, ω (m^3) the van der Waals' volume of a fission gas atom, $n_{a,gb}$ (/) the number of fission gas atoms per bubble, Ω (m^3) the atomic (vacancy) volume in the bubble, and $n_{v,gb}$ (/) the number of vacancies per bubble. The gas atom inflow rate at the bubble, $\mathrm{d}n_{a,gb}/\mathrm{d}t$, is obtained from Eq. 52. The vacancy absorption/emission rate at the bubble, $\mathrm{d}n_{v,gb}/\mathrm{d}t$, is calculated using the model of Speight and Beere [28], i.e.,

$$\frac{\mathrm{d}n_{v,gb}}{\mathrm{d}t} = \frac{2\pi D_{gb}^{v}\delta_{gb}}{kTS}\left(p_{gb} - p_{gb,eq}\right) \tag{59}$$

where D_{gb}^{v} ($m^2 s^{-1}$) is the vacancy diffusion coefficient along grain boundaries, δ_{gb} (m) the thickness of the diffusion layer in grain boundaries, and the parameter S depends on the fraction of grain faces covered by bubbles (fractional

coverage) as detailed in [29]. The pressure of the gas in the bubble, p_{ig} (Pa), is calculated based on the van der Waals equation of state. The mechanical equilibrium pressure, $p_{gb,eq}$ (Pa), is given by

$$p_{gb,eq} = \frac{2\gamma}{R_{gb}} - \sigma_h \tag{60}$$

where R_{gb} the bubble radius of curvature, which is calculated as

$$R_{gb} = \left(\frac{3V_{gb}}{4\pi\varphi(\theta)} \right)^{1/3} \tag{61}$$

where $\varphi = 1 - 1.5\cos(\theta) + 0.5\cos^3(\theta)$ is the geometric factor relating the volume of a lenticular bubble to that of a sphere, and θ is the bubble semi-dihedral angle. A value of 72.9° for the bubble semi-dihedral angle is considered in the model, which is based on the recent molecular dynamics calculations in [70].

Grain-boundary bubble coalescence is described using an improved model of White [29, 30]. The variation rate due to coalescence of the bubble number density, N_{gb} (m^{-2}), is calculated as a function of the variation rate of the bubble projected area on the grain face, $A_{gb} = \pi R_{gb}^2$ (m^2). More details are given in [30]. A lower limit $N_{gb,low} = 10^{10}$ m^{-2} is set.

Under the above assumptions, the fractional volumetric inter-granular fission gas swelling is given by

$$\left(\frac{\Delta V}{V}\right)_{gb} = \frac{1}{2}\frac{3}{r_{gr}} N_{gb} V_{gb} \tag{62}$$

where V (m^3) is the fuel volume, r_{gr} (m) the grain radius, and $3/r_{gr}$ represents the grain surface to volume ratio.

Thermal FGR is modeled based on a principle of grain face saturation. More precisely, after the fractional coverage attains a saturation value, $F_{c,sat}$, further bubble growth is compensated by gas release in order to maintain the constant coverage condition

$$\frac{dF_c}{dt} = \frac{d\left(N_{gb}A_{gb}\right)}{dt} = 0 \qquad if \;\; F_c = F_{c,sat} \tag{63}$$

3.5.2 Atomistic Model for Diffusivities

Atomistic calculations were recently performed at Los Alamos National Laboratory for the calculation of the diffusivities of gas atoms (Xe) and vacancies in U_3Si_2, i.e., the parameters D and D_{ig}^v, respectively, in the model described above. An account of the atomistic calculations is given hereinafter.

Similarly to UO_2 self-diffusion and Xe diffusion in U_3Si_2 exhibits three diffusion regimes. In previous work [72], DFT was used to investigate the intrinsic diffusion regime for Xe, Si interstitials, Si vacancies, U interstitials, and U vacancies. Xe diffusivity was predicted to be significantly higher in U_3Si_2 than in UO_2 for a given temperature and exhibited a small degree of anisotropy due to the different diffusion mechanisms in the *aa* and *cc* directions of the tetragonal U_3Si_2 lattice. For both Si and U, interstitial diffusion dominates over vacancy diffusion. However, for intergranular bubble swelling it is vacancy diffusion that is most important. To enable the stoichiometric growth of bubbles both U and Si vacancies must arrive. Given the rapid diffusion of U vacancies, Si vacancy diffusivity is treated as the rate limiting process for bubble swelling. The DFT modeling predicted that a significant amount of excess Si can be accommodated in U_3Si_2, therefore the diffusivities were calculated for Si-rich as well as stoichiometric conditions. Following a similar approach to that carried out on UO_2 [73], classical molecular dynamics (MD) simulations using the U_3Si_2 interatomic potential developed by Beeler et al. [74] were used to predict the athermal, D_3, fission gas diffusivity during ballistic damage cascades. In the fission gas model the highest Xe diffusivity (*aa* or *cc*) should be used in combination with the highest Si vacancy diffusivity (*aa* or *cc*), as summarized by Eqs. (64) to (67). Due to the inclusion of Xe athermal diffusion in Eqs. (64) and (66) the model can be applied over a wide range of temperatures and fission rates. Note that D_3 is excluded from vacancy diffusion given that the disorder during a cascade means that tracking the displacement of individual vacancies loses its meaning.

Stoichiometric conditions:

$$D = 2.853 \times 10^{-4} exp\left(\frac{-3.173 \text{ eV}}{k_B T}\right) + 3.58 \times 10^{-42} \dot{F} \tag{64}$$

$$D_{ig}^{v} = 9.393 \times 10^{-4} exp\left(\frac{-4.167 \text{ eV}}{k_B T}\right) \tag{65}$$

Si-rich conditions:

$$D = 7.224 \times 10^{-6} exp\left(\frac{-2.836 \text{ eV}}{k_B T}\right) + 3.58 \times 10^{-42} \dot{F} \tag{66}$$

$$D_{ig}^{v} = 9.762 \times 10^{-4} exp\left(\frac{-4.217 \text{ eV}}{k_B T}\right) \tag{67}$$

where D and D_{ig}^{v} represents Xe and Si vacancy diffusivities, respectively, in $m^2 s^{-1}$, and $\dot{F}$ is the fission rate density in $s^{-1} \cdot m^{-3}$.

3.5.3 Applicability and Uncertainty

The U_3Si_2 fission gas behavior model described above is applicable to normal operating conditions of LWRs. Specific validation data will be necessary in order to qualify the model for usage for analyzing off-normal conditions.

Significant uncertainties exist in several parameters of the fission gas model, which are discussed in [69]. Additional discussion is provided in Section 5.2. As for the uncertainty in the diffusivities calculated through atomistic modeling (Section 3.5.2), given that intermediate irradiation enhanced, D_2, diffusion is not yet included there is uncertainty near the D_1-D_3 transition in Eqs. (64) and (66). Due to the possibility of excess Si in U_3Si_2 fuel the difference between the stoichiometric model, Eqs. (64) and (65), and the Si-rich model, Eqs. (65) and (67), represents further uncertainty. This latter aspect is accounted for in the sensitivity analysis presented in Section 5.2.

3.6 Solid Swelling (`U3Si2VolumetricSwellingEigenstrain`)

3.6.1 Model Development

The solid swelling is a linear function of burnup based upon the data of [75]. To convert the data (fission density) to FIMA, a value of 10.735 g/cm^3 was used as the heavy metal density, equivalent to 95% theoretical heavy metal density yielding a conversion factor of 3.63457×10^{-23}.

$$\left(\frac{dV}{V}\right)_{solid} = 0.34392 \times Bu \tag{68}$$

where Bu is the burnup in FIMA.

3.6.2 Applicability and Uncertainty

The correlation for solid swelling of U_3Si_2 is valid over burnups spanning the entire life of the fuel under typical LWR conditions. The uncertainty in the model is unknown. As a conservative assumption the uncertainty in the solid swelling model for UO_2 [16] in Bison is used because the form of that equation is similar to Equation 68 (i.e., a linear function of burnup). Therefore, an uncertainty range (95% confidence interval of a Gaussian distribution) of $\pm$20% is considered in line with [10]. This is also compatible with the uncertainty estimated in [1].

3.7 Gaseous Swelling (U3Si2VolumetricSwellingEigenstrain)

3.7.1 Model Options

FINLAY Model

A legacy model in Bison is based upon an empirical expression determined using data from [76] by [53]. The swelling of fuel particles was calculated using the results of miniplate irradiation tests. To convert the data from fission density into burnup in FIMA the same conversion factor for solid swelling was used (i.e.,3.63457×10^{-23}) . The total volumetric strain due to fission products is then given by

$$\frac{dV}{V} = 3.8808 \times Bu^2 + 0.79811 \times Bu \tag{69}$$

where dV/V is the volumetric strain at a given burnup Bu in FIMA. The quadratic equation for the total volumetric strain is then decoupled into its solid and gaseous components. The solid swelling is a linear function of burnup as described in section 3.6.1. This equation is substracted from the total volumetric strain given by Equation 69 to give the gaseous swelling component

$$\left(\frac{dV}{V}\right)_{gaseous} = 3.8808 \times Bu^2 + 0.45419 \times Bu \tag{70}$$

ARGONNE Model

Another model for computing gaseous swelling component utilizes the rate theory calculations by [61]. A look-up table in temperature (T), temperature gradient (G), and fission density (f) was derived that predicts the amount of gaseous swelling in U_3Si_2. Between values within the look-up table tricubic interpolation is used for improved continuity.

COUPLED Model

The coupled model refers to the inherently coupled phenomena of fission gas release and gaseous swelling, as fission gas release from the grain faces counteracts bubble growth and thereby results fission gas swelling. The total gaseous swelling according to the fission gas behavior model described in Section 3.5 is calculated as the sum of the intra-granular (Equation 57) and inter-granular contributions (Equation 62)

$$\left(\frac{\Delta V}{V}\right)_{gaseous} = \left(\frac{\Delta V}{V}\right)_{ig} + \left(\frac{\Delta V}{V}\right)_{gb} \tag{71}$$

3.7.2 Applicability and Uncertainty

The FINLAY model is applicable for all burnups under normal operating LWR conditions. The ARGONNE has the same ranges of applicability as the thermal conductivity degradation model based upon rate theory calculations. The model is a function temperature (T), temperature gradient (G), and fission density (f), which each have the following ranges of applicability:

$390 \leq T \leq 1190$ K

$0 \leq G \leq 160$ K/mm

$0 \leq f \leq 2.5755 \times 10^{21}$ fissions/cm^3

The COUPLED model has the same range of applicability as the fission gas release model described in Section 3.5 (i.e., normal operating conditions of LWRs).

3.7.3 Model Recommendation

The `COUPLED` is recommended because of the intimately related phenomena of fission gas release and gaseous swelling, and of the models currently available in Bison, it is the only one that takes the coupling into account.

3.8 Densification (`U3Si2VolumetricSwellingEigenstrain`)

3.8.1 Model Choice

The densification behavior of U_3Si_2 is currently unknown. In absence of other data the model available in Bison for UO_2 is used as per [53]. The model in Bison for modeling of densification of UO_2 is a modified version of the ESCORE model described in [40]. Typically, the default value of 1% theoretical density is taken as the maximum amount of densification that can occur. This is currently assumed for U_3Si_2 as well.

3.8.2 Applicability and Uncertainty

The ESCORE densification model is applicable for all normal operating temperatures and burnups experienced by fuel within a LWR. Uncertainty in the model is not currently available. Further work is required to improve understanding of the densification phenomenon in U_3Si_2.

4 Validation

4.1 Cr_2O_3-doped UO_2

Validation of Bison for Cr_2O_3-doped UO_2 was performed to integral fuel rod experiments in the IFA-677.1 and IFA-716.1 tests performed at the Halden Reactor Project [43, 44]. In the following, a brief description of the tests and comparisons of the Bison predictions to the available experimental data of fuel centerline temperature, fission gas release and rod inner pressure is provided.

4.1.1 Description of Halden Fuel Rod Tests IFA-677.1 and IFA-716.1

The Halden test IFA-677.1 [41, 43, 44] aimed to investigate the performance of modern fuels subjected to high initial rating. The test rig contained six rods. Two of the rods, supplied by Westinghouse, contained UO_2 fuel doped with Cr_2O_3 and Al_2O_3. All rods were instrumented with pressure transducers and fuel centerline thermocouples in both ends. The test was loaded in the Halden reactor in December 2004 and completed six cycles of irradiation under HBWR (Halden Boiling Water Reactor) conditions in September 2007, achieving a rig average burnup of ∼26.3 MWd/kgOX. Rods 1 and 5 from the IFA-677.1 test, i.e., the ones fueled with Cr_2O_3-doped UO_2, have been simulated with Bison.

The test IFA-716.1 [6, 42, 45] is a continuation of IFA-677, performed to investigate the effects on fission gas release of Cr_2O_3 dopant concentration and UO_2 grain size. IFA-716.1 contained a cluster of six rods, all instrumented with pressure transducers and fuel centerline thermocouples at the upper end of the fuel stack. The rig was loaded in the Halden reactor in January 2010 and completed 12 irradiation cycles under HBWR conditions in mid 2014, achieving a rig average burnup of 27 MWd/kgOX. The rig was subsequently reloaded as IFA-716.2 and irradiated for three more cycles. Rod 1 in IFA-716.1, manufactured from the fuel supplied by AREVA, was one of two rods containing Cr_2O_3-doped UO_2 fuel and is considered in the present work. The IFA-716.2 irradiation beyond the 12th cycle [6] is not considered here and would not allow for additional comparisons to rod pressure or FGR measurements, because the pressure transducer in rod 1 failed before the end of the IFA-716.1 irradiation.

The main characteristics of the fuel rods in IFA-677.1 and IFA-716.1 simulated in the present work are summarized in Table 4.

Table 4: Fabrication characteristics of IFA-677.1 and IFA-716.1 rods simulated in this work [6, 41–45]

		IFA-677.1 rod 1	IFA-677.1 rod 5	IFA-716.1 rod 1
Cladding material		Zircaloy-4	Zircaloy-4	Zircaloy-4
Fuel material		UO_2 + additives	UO_2 + additives	UO_2 + additives
Fill gas		He	He	He
Total active fuel stack length	mm	398.6	403.5	399.5
Drilled active section length (top)	mm	109.2	111.0	115
Drilled active section length (bottom)	mm	109.7	111.1	-
Pellet inner diameter (drilled sections)	mm	1.8	1.8	1.8
Pellet outer diameter	mm	9.13	9.13	9.12
Diametral gap	μm	170	170	180
Cladding thickness	mm	0.725	0.725	725
Cladding outer diameter	mm	10.75	10.75	10.75
Free volume	cm^3	5.34	5.26	5.80
Fill gas pressure	MPa	1.35	1.35	1
Fuel Cr_2O_3 content	ppm	900	500	1580
Fuel Al_2O_3 content	ppm	200	200	-
Fuel U-235 enrichment	%	4.94	4.91	4.90
Initial fuel density	kg/m^3	10690	10700	10500
Fuel average grain radius	μm	28	22.5	35

The average linear heat rate (LHR) histories for the fuel rod test in IFA-677.1 and IFA-716.1 analyzed in this work are illustrated in Figure 8. The Halden raw data was condensed using the Fuel Rod Analysis ToolBox developed by K. Lassmann [77]. The thermal boundary conditions at the cladding outer surface were determined using Bison's internal coolant channel model, with the coolant inlet temperature history determined from the Halden raw data. The Jens-Lottes heat transfer correlation, which is recommended for Halden HBWR conditions was applied.

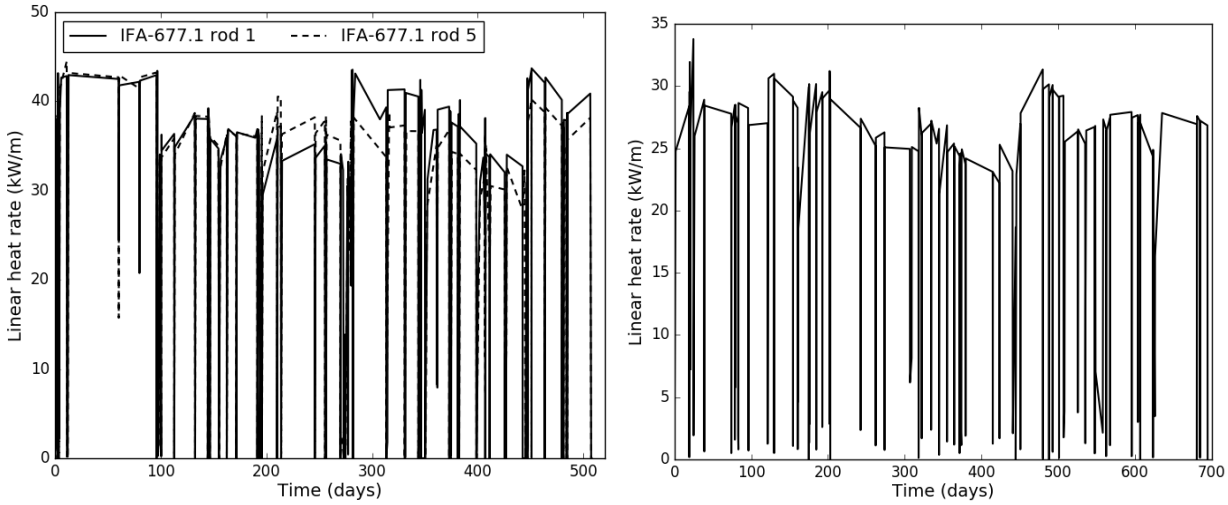

Figure 8: Average linear heat rate histories for (a) IFA-677.1 rods 1, 5 and (b) IFA-716.1 rod 1.

4.1.2 Results Comparisons to Experimental Data

IFA-677.1 rod 1

For IFA-677.1 rod 1, the comparisons of calculated and measured fuel centerline temperature evolutions at upper and lower thermocouple positions are shown in Figures 9(a) and 9(b), respectively. For both positions, the Bison calculation matches the experimental data well for the first 3 cycles of irradiation. An overprediction of the measured temperature of up to ∼100 K is observed for the fourth and fifth cycles. Such a discrepancy corresponds to a relative error of ∼7%, which is comparable to the uncertainties in the rod linear power data used as input for the calculation. For the sixth cycle, a more severe overprediction of up to ∼300 K is observed. Discrepancies are expected to be largely associated with errors in the Halden linear heat rate data used as input for the simulations. In particular, as discussed at a recent Enlarged Halden Programme Meeting [78], the linear heat rate provided by Halden is expected to be overestimated during approximately the second half of the irradiation. This seems consistent with the overprediction of the fuel temperature observed for the Bison simulation during the last 3 irradiation cycles.

The calculated fission gas release as a function of rod average burnup is shown in Figure 10 along with the measured data (which are inferred from the inner rod pressure on-line measurement [43]). Overall, FGR is predicted accurately, both in terms of kinetics and end-of-life value. In particular, Bison predicts a FGR of ∼17% at the end of life, with the experimental value being 22%. The discrepancy can be considered low, in view of the inherent modeling uncertainties for FGR [21].

In Figure 11, the time evolution of rod inner pressure calculated by Bison is compared to the on-line experimental data from the pressure transducer. Overall, the prediction appears reasonably accurate, although a moderate overprediction of the measured rod inner pressure is observed. Discrepancies may be partly due to inaccuracies in the calculation of the plenum temperature, which is a known issue for the prediction of fuel rod inner pressure with fuel performance codes [79].

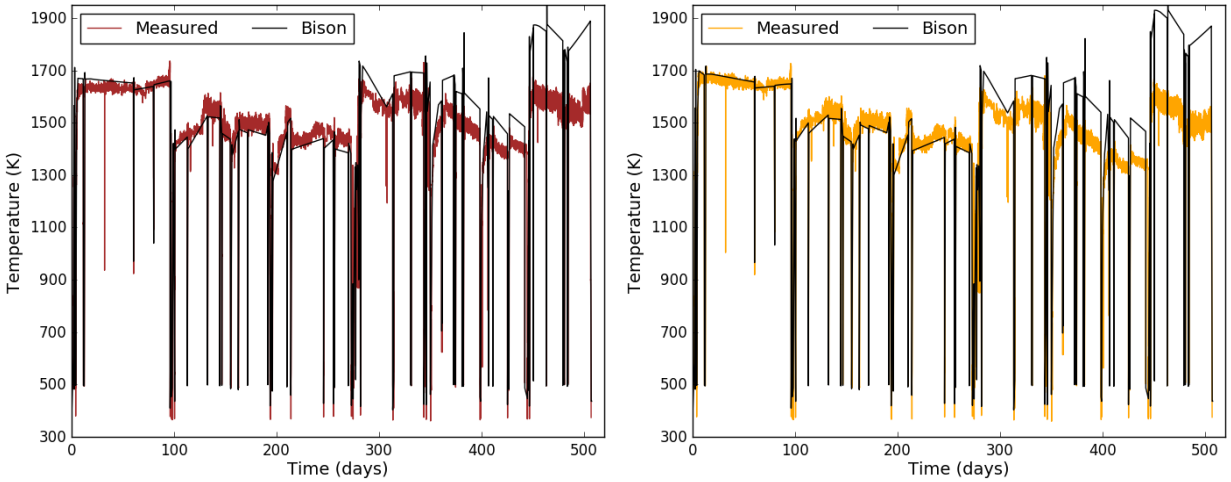

Figure 9: Comparison of predicted and measured fuel centerline temperature histories at the (a) upper and (b) lower thermocouple locations for IFA-677.1 rod 1.

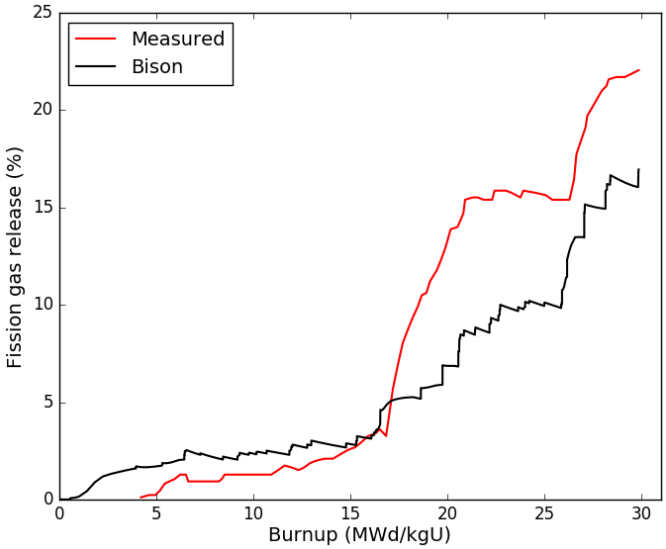

Figure 10: Comparison of predicted and measured fission gas release as a function of rod average burnup for IFA-677.1 rod 1.

IFA-677.1 rod 5

Comparisons of Bison calculations to in-pile data for IFA-677.1 rod 5 are presented in Figures 12 to 14. Similar considerations to those made for rod 1 can be derived.

Fuel centerline temperature predictions (Figures 12(a) and 12(b)) are in general accurate for the first five cycles of irradiation, with a significant overprediction observed during the sixth cycle. The discrepancies remain below ~80K during the first five cycles for both comparisons at the upper and lower thermocouple locations. During the sixth cycle, maximum discrepancies of ~100 K at the upper location and ~200 K at the lower location are observed. As mentioned above, discrepancies are expected to be largely associated with errors in the input linear heat rate data [78].

The FGR prediction (Figure 13) is accurate. In particular, Bison predicts a FGR of ~13% at the end of life, which is close the measured value of 16% from puncturing [44]. The kinetics of FGR also appears to be reproduced with a good

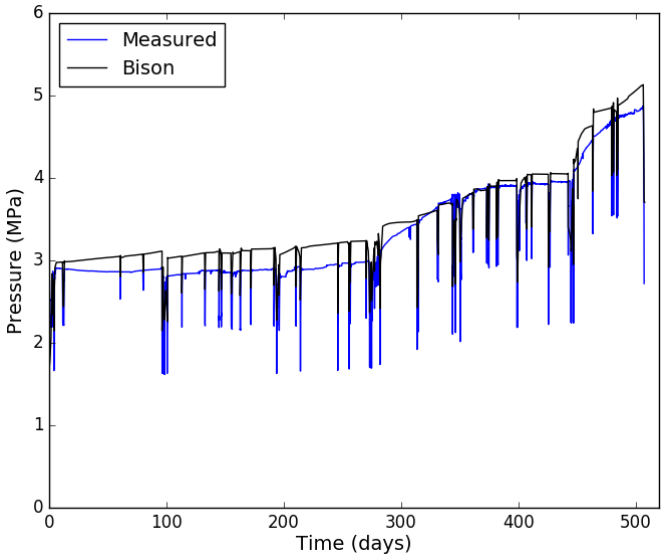

Figure 11: Comparison of predicted and measured inner rod pressure histories for IFA-677.1 rod 1.

accuracy, although Bison predicts an earlier onset of FGR compared to the experimental data. It is noted, however, that the FGR on-line data are inferred from the rod pressure measurements and the onset of FGR is set based on the Halden (Vitanza) threshold rather than being a direct measurement of the onset of FGR [43].

As for the rod inner pressure (Figure 14), the calculation reproduces the measured data with good accuracy, although a moderate underprediction is observed. As commented above, it is expected that discrepancies be partly due to inaccuracies in the calculation of the plenum temperature.

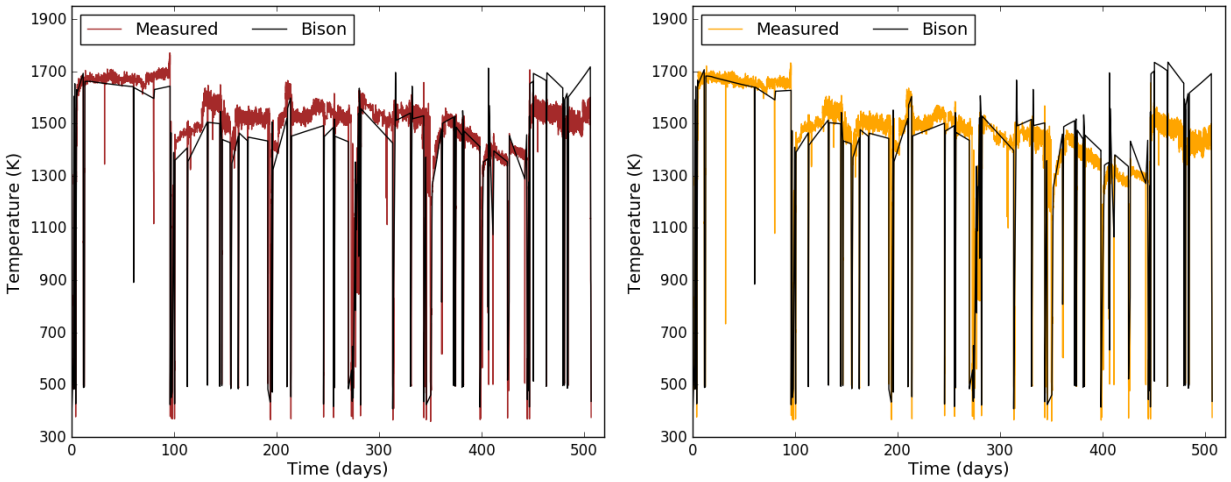

Figure 12: Comparison of predicted and measured fuel centerline temperature histories at the (a) upper and (b) lower thermocouple locations for IFA-677.1 rod 5.

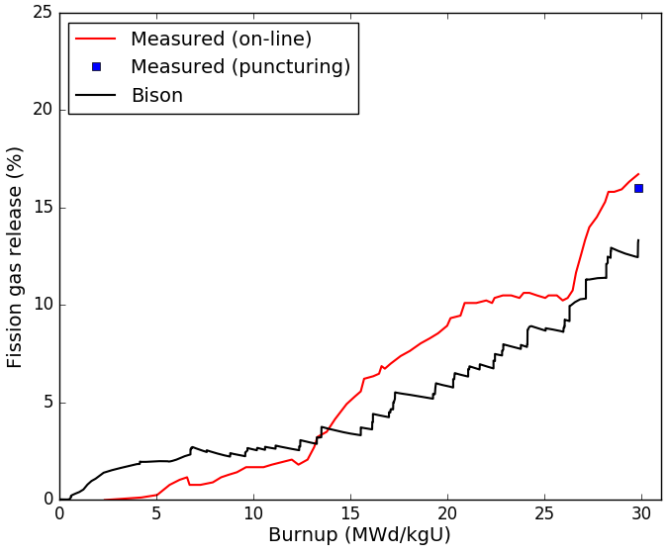

Figure 13: Comparison of predicted and measured fission gas release as a function of rod average burnup for IFA-677.1 rod 5.

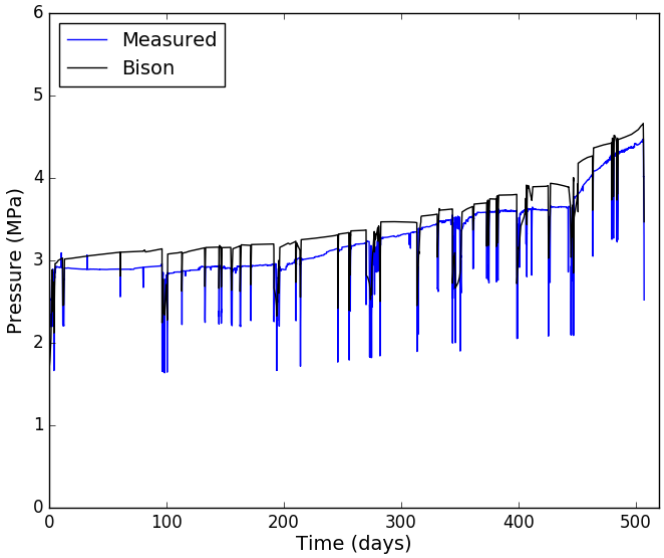

Figure 14: Comparison of predicted and measured inner rod pressure histories for IFA-677.1 rod 5.

IFA-716.1 rod 1

The comparison of calculated and experimental fuel temperature at the thermocouple location for IFA-716.1 rod 1 is illustrated in Figure 15. The Bison calculation systematically underpredicts the measured data by ∼100K throughout the irradiation. Such a discrepancy corresponds to a relative error of ∼7-8%, which is comparable to the uncertainties in the rod power data used as input for the calculation.

The calculated and experimental FGR for IFA-716.1 rod 1 are shown in Figure 16 as a function of rod average burnup. The experimental data are inferred from the rod inner pressure measurements. Because the pressure transducer failed after approximately 620 days of irradiation [6], data are shown only until the point of sensor failure. As with the IFA-677.1 rods (Figures 10, 13), Bison predicts an earlier onset of FGR than indicated by the data from measurements. As commented above, however, the onset of FGR in the experimentally derived data is set based on the Vitanza threshold rather than being a direct measurement. The end-of-life value of FGR is underpredicted by Bison, with the calculated

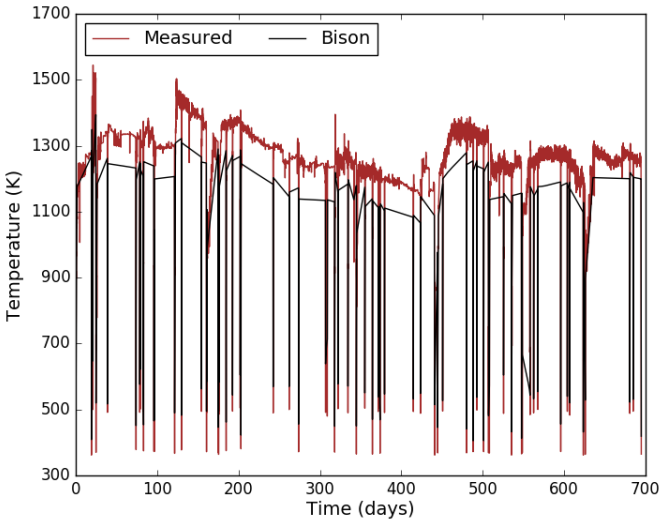

Figure 15: Comparison of predicted and measured fuel centerline temperature histories for IFA-716.1 rod 1.

value being ∼2.7% and the value from measurement being ∼5.6% (i.e., an error of a factor of ∼2). This discrepancy can be partly attributed to the underprediction of fuel temperature (Figure 15), as FGR is strongly temperature-dependent. Note, however, that a prediction error of up to a factor of 3 can be considered acceptable for FGR, in view of the inherent modeling uncertainties [21]. In addition to this, there is a significant uncertainty in the experimental value, which for IFA-716.1 rod 1 has been estimated as ∼1.4% FGR at the end of life in [6].

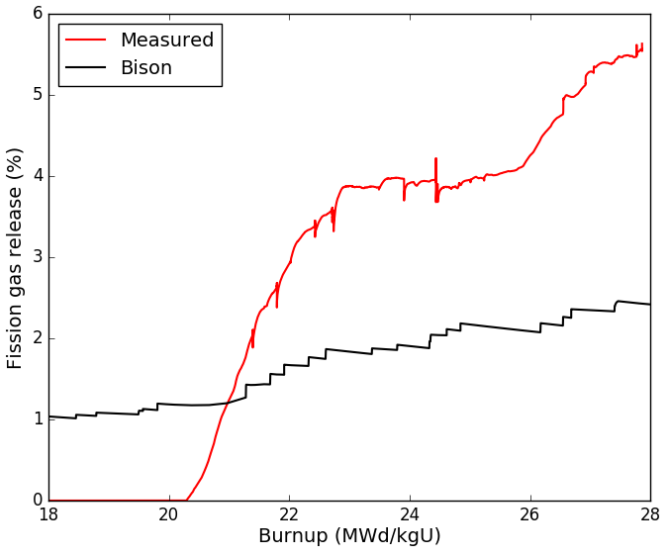

Figure 16: Comparison of predicted and measured fission gas release as a function of rod average burnup for IFA-716.1 rod 1. Data are only shown until the point of sensor failure.

The comparison of calculation to experimental data of rod inner pressure is shown in Figure 17. Overall, the Bison prediction is accurate, although a moderate underprediction of the data is observed.

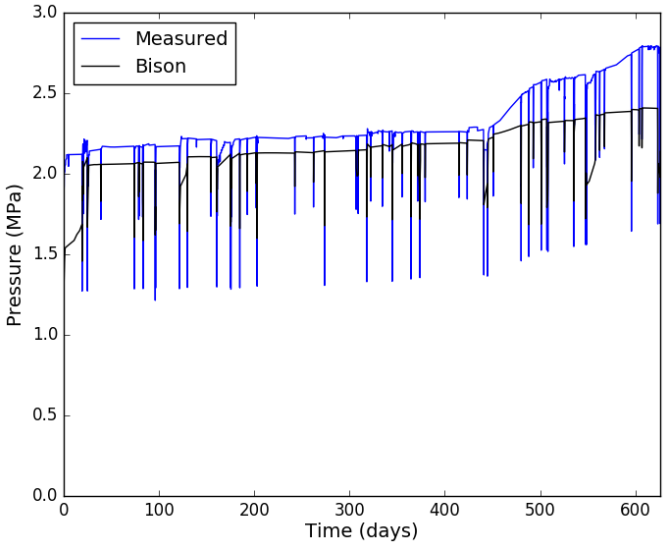

Figure 17: Comparison of predicted and measured inner rod pressure histories for IFA-716.1 rod 1. Data are only shown until the point of sensor failure.

4.2 U_3Si_2

Validation of Bison for U_3Si_2 fuel behavior was performed to recent PIE data for the ATF-13 R4 and ATF-15 R6 rodlets irradiated in the ATR at Idaho National Laboratory. These simulations are to the authors' knowledge, the first validation of U_3Si_2 fuel performance models. The experiments were designed to investigate the low-burnup behavior of U_3Si_2. In particular, the axial elongation of the fuel stack, cladding outer diameter, and fission gas release were of interest. The following subsection describes the experiment as well as the initial Bison predictions to fuel elongation and fission gas release.

4.2.1 ATF-13 R4 and ATF-15 R6

The ATF-1W ATR experimental program contained six fuel rods to investigate the performance behavior of U_3Si_2 fuel under LWR conditions [80]. PIE has been completed on two rods identified as R4 from the ATF-13 capsule and R6 from the ATF-15 capsule [2]. The experiments are a typical capsule irradiation test, which consists of a fuel rodlet encapsulated inside of a stainless steel capsule. The nominal dimensions of all capsules used in the ATF-1 experiments are shown in Figure 18. Specific details for the R4 and R6 rodlets can be obtained from the design specifications of the experiments. The R4 and R6 rodlets consisted of 12 enriched (5.44wt% U-235) U_3Si_2 stacked on top of a single depleted pellet with an additional two depleted placed on top of the active length. The top two depleted pellets were drilled to accommodate melt wires to monitor the temperature during the experiment. In these experiments, the fuel was placed inside ZIRLO^{TM} before being inserted into the stainless steel capsule. Details on the fabrication of the fuel pellets is discussed by Harp et al. [81].

The power supplied to the fuel rodlets as a function of time is shown in Figure 19. A flat axial profile was assumed in the Bison simulation given the short length of the rodlet. The rodlets were removed from the ATR at a relatively low burnup (17.1 MWd/kgHM for R4 and 19.6 MWd/kgHM for R6 [2]) to perform PIE. For engineering scale simulation comparisons limited data exists. Previous experience from research reactor irradiations of U_3Si_2 suggested that at some point the fuel will experience runaway swelling. Therefore, measurements focused on dimensional changes of the fuel and clad, and fission gas release. Measurements of fuel dimensional changes were limited to neutron radiography that illustrated that the fuel experienced no axial growth (elongation) to the resolution of the measurement technique. Cladding profilometry measurements indicated negligible change from the as-fabricated dimensions meaning that no contact between the fuel and clad was observed.

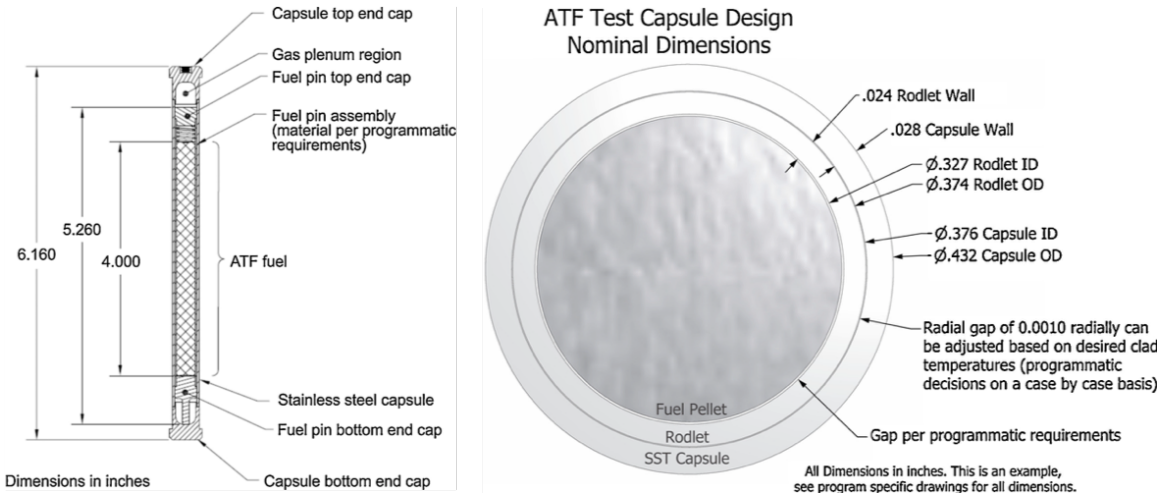

Figure 18: ATF-1 test capsule assembly (left) and capsule cross-section (right). Images reproduced from Barrett et al. [80].

Simulation comparisons to the experimental values for fuel elongation and fission gas release are tabulated in Table 5. For the R4 rodlet Bison predicts a negative fuel elongation indicating that densification of the fuel was not overcome by solid and gaseous swelling. For the R6 case, which operated at higher temperatures the Bison prediction indicates a small amount of axial elongation. Fission gas release was underpredicted for the R4 rodlet and overpredicted for the R6 rodlet. However, given the inherent uncertainties in the modeling of fission gas behavior (See Section 5.2) [21] these initial predictions are reasonable. The Bison simulations predicated no pellet clad mechanical interaction and therefore no cladding dimensional changes, consistent with the experimental results.

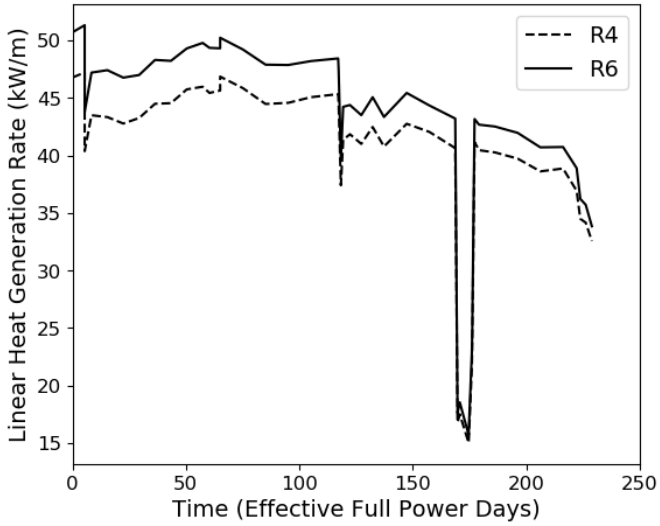

Figure 19: Linear heat generation rate supplied to ATR-13 R4 and ATR-15 R6. Adapted from Cappia and Harp [2].

Table 5: Bison comparisons to PIE data for ATF-13 R4 and ATF-15 R6 [82].

	Bison R4	Experiment R4	Bison R6	Experiment R6
Fuel Elongation (mm)	-0.0784	0.0	0.0128	0.0
Fission Gas Release (%)	0.0	0.06	0.19	0.06

5 Uncertainty Quantification and Sensitivity Analysis

In this chapter, the IFA-716 rod 1 and ATF-13 R4 rodlets were selected to perform more detailed uncertainty quantification sensitivity analysis for Cr_2O_3-doped UO_2 and U_3Si_2, respectively. Selected model inputs have been varied with their associated uncertainties described in Chapters 2 and 3 . Uncertainty quantification is given by providing the range of of values predicted by Bison with $\pm 2\sigma$ about the mean. In the case of fission gas release the lower bound of the range is fixed at zero if two standard deviations below the mean would result in a negative value of FGR. Sensitivity analysis is completed by investigating the Spearman correlation coefficients, which indicate monotonic relationships between the figures of merit and the uncertain inputs. The uncertainty quantification and sensitivity analysis studies are completed by coupling Bison to the Dakota [83] software developed at Sandia National Laboratories.

5.1 Cr_2O_3 Doped UO_2

5.1.1 Uncertain Parameters and Sensitivity Ranges

The parameters considered in the sensitivity analysis for Cr_2O_3-doped UO_2 are reported in Table 6 along with the considered nominal values and ranges of variation. Where normal or lognormal distributions are considered, the range of variation is intended as $\pm 2\sigma$, i.e., 95% confidence interval.

For thermal conductivity, thermal expansion strain, solid swelling and total densification, the nominal values and ranges of variation are as discussed in Chapter 2.

The intra-granular diffusion coefficient of gas atoms, re-solution rate of intra-granular bubbles and inter-granular diffusion coefficient of vacancies are parameters of the fission gas model (Section 2.4) and affect fuel gaseous swelling through Eq. 17. Also, the grain radius affects both fission gas release and swelling through the fission gas model. In particular, the grain radius affects (i) the average diffusion distance for gas atoms, hence the rate of gas transport to the grain boundaries and ultimately FGR and swelling due to inter-granular bubbles, and (ii) the grain surface to volume ratio, hence the capacity of the grain faces to store fission gas. There is also a direct effect of the grain radius on gaseous swelling, as seen in Eq. 17. Hence, these four parameters are considered to represent the uncertainty in both fission gas swelling and release. The choice of the parameters and the corresponding ranges of variation are based on a previous sensitivity analysis of the Bison fission gas model both in terms of fission gas release and gaseous swelling [21]. For the grain radius, although further confirmation is needed on the uncertainty specific to grain size evolution in Cr_2O_3-doped UO_2, the estimate from [21] is maintained here to account for the existing uncertainty in the grain radius used on the calculations, in a preliminary way.

Table 6: Parameters considered in the sensitivity analysis for Cr_2O_3-doped UO_2 and corresponding ranges of variation.

Parameter	Nominal value	Scaling factor range	Distribution
Thermal conductivity ($W{\cdot}m^{-1}K^{-1}$)	See Equation 1	[0.9; 1.1]	Normal
Thermal expansion strain (K^{-1})	See Equation 4	[0.85; 1.15]	Normal
Solid swelling (/)	See Equation 18	[0.8; 1.2]	Normal
Total densification (/)	0.002	[0; 5]	Uniform
Intra-granular diffusion coefficient of gas atoms ($m{\cdot}s^{-2}$)	See Equation 8	[0.1; 10]	Lognormal
Re-solution rate from intra-granular bubbles (s^{-1})	See Equation 10	[0.1; 10]	Lognormal
Inter-granular diffusion coefficient of vacancies ($m{\cdot}s^{-2}$)	See Equation 14	[0.1; 10]	Lognormal
Grain radius (m)	See Equation 5	[0.4; 1.6]	Normal

5.1.2 Results and Discussion: IFA-677.1 Rod 1

For the sensitivity analysis of Cr_2O_3-doped UO_2 fuel modeling, the considered case is the Halden test IFA-716.1 rod 1 (Section 4.1.1). For the reference Bison calculation, the settings are the same as used in the validation study presented in Section 4.1.2.

The results of the sensitivity analysis in terms of Spearman correlation coefficients are presented in Figure 20. Considered figures of merit are integral FGR in the fuel rod and fuel stack elongation, both at the end of life.

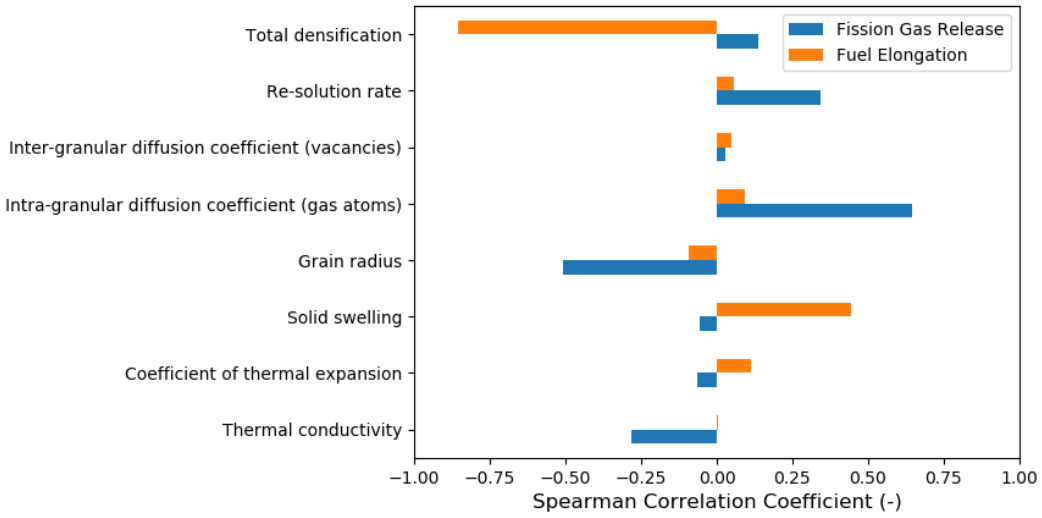

Figure 20: Spearman correlation coefficients for the sensitivity analysis of the Cr_2O_3-doped UO_2 case IFA-716.1 rod 1.

The parameters having the largest effect on FGR are the intra-granular diffusion coefficient of gas atoms and the grain radius. The re-solution rate from intra-granular bubbles and the fuel thermal conductivity also have a significant effect on FGR.

The intra-granular diffusion coefficient determines the arrival rate of gas atoms to grain boundaries, which is a rate limiting mechanism for swelling due to inter-granular bubbles and the eventual FGR (Section 2.4). Hence the positive correlation of the intra-granular diffusion coefficient with both FGR and fuel elongation. The grain radius determines the average intra-granular diffusion distance, hence, it also affects FGR and gaseous swelling through the arrival rate of gas atoms to grain boundaries. In particular, a larger grain radius results in a higher diffusion distance and reduced diffusion rate to grain boundaries, which results in a negative correlation of the grain radius to FGR and fuel elongation. The suppression of FGR with larger grains is one of the main potential advantages of Cr_2O_3-doped UO_2. The re-solution rate from intra-granular bubbles affects the effective intra-granular diffusion coefficient of gas atoms (Eq. 7). In particular, a higher re-solution rate corresponds to a higher rate of gas transport to grain boundaries, which in turn favors FGR and gaseous swelling due to grain-boundary gas bubbles (Section 2.4). Hence the positive correlation of the re-solution rate with both FGR and fuel elongation (although the latter effect is small). FGR being strongly temperature-dependent, the fuel thermal conductivity affects FGR through fuel temperature. In particular, a higher thermal conductivity results in lower fuel temperatures and FGR. The positive correlation of densification with FGR is ascribed to a larger gap and consequently, higher fuel temperatures and FGR correspond to a higher densification.

The parameters having the largest effect on fuel stack elongation at the end of life are the total densification and solid swelling. Both parameters affect the fuel elongation through directly affecting the fuel volume. As expected, densification is negatively correlated to fuel elongation, while correlation with solid swelling is positive. Also, thermal expansion also has a direct (and positive) effect on fuel elongation. In addition to the indirect effect of grain radius on gaseous swelling through the diffusion distance mentioned above, the negative correlation of the grain radius to fuel elongation is also through the grain surface to volume ratio, which directly affects gaseous swelling through Eq. 17.

Time-dependent results are presented in Figure 21 in terms of $\pm 2\sigma$ on the mean value of the calculated fuel temperature at the thermocouple location for IFA-716.1 rod 1. Experimental data are also included. While the time-dependent mean value of the calculated temperature underpredicts the experimental data, the upper bound of the $\pm 2\sigma$ envelope is very close to the data. Hence, these results indicate that inherent modeling uncertainties considered may explain the underestimation of the fuel temperature for IFA-716.1 rod 1 observed in Section 4.1.2.

In Figure 22, time-dependent results in terms of $\pm 2\sigma$ on the mean value of the calculated FGR for IFA-716.1 rod 1 are illustrated. Experimental data are also included. The lower bound of the $\pm 2\sigma$ envelope equals zero FGR. FGR

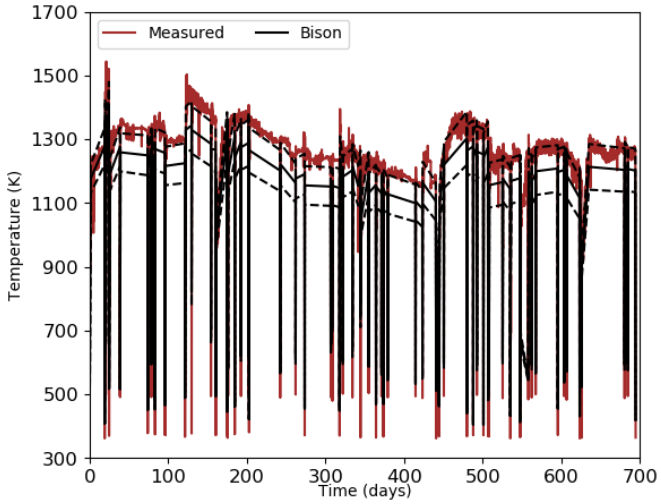

Figure 21: Temperature history including $\pm 2\sigma$ on the mean value for the uncertainty quantification of the Cr_2O_3-doped UO_2 case IFA-716.1 rod 1.

being a threshold phenomenon, this corresponds to the limit for the onset of FGR not being attained (see Section 2.4). The upper bound of the envelope is relatively close to the experimental data. Note that experimental FGR data are inferred from the rod pressure measurements, and there is a significant uncertainty in the data, which for IFA-716.1 rod 1 has been estimated as ∼1.4% FGR at the end of life in [6]. Considering also the experimental uncertainty, the data fall within the estimated 95% confidence interval of the calculation. Therefore, also in this case, results indicate that inherent modeling uncertainties may explain the underestimation of FGR for IFA-716.1 rod 1 observed in Section 4.1.2.

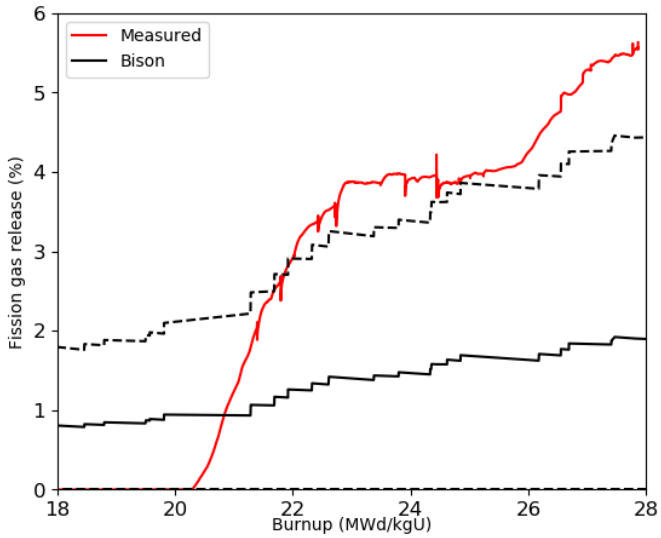

Figure 22: Fission gas history including $\pm 2\sigma$ on the mean value for the uncertainty quantification of the Cr_2O_3-doped UO_2 case IFA-716.1 rod 1.

5.2 U_3Si_2

5.2.1 Uncertain Parameters and Sensitivity Ranges

The parameters considered in the sensitivity analysis for U_3Si_2 are reported in Table 7 along with the considered nominal values and ranges of variation. Ranges of variation are discussed in Chapter 3.

For thermal conductivity, coefficient of thermal expansion, elastic constants, and solid swelling rate, normal distributions are considered, and the range of variation is intended as $\pm 2\sigma$, i.e., 95% confidence interval.

For the parameters of the fission gas behavior model (i.e., the calculation of gaseous swelling and fission gas release), the choice of the parameters and ranges of variation is based on the previous sensitivity analysis perfomed in [69]. In particular:

- The uncertain parameters that were associated with the highest sensitivity coefficients according to the analysis in [69] were selected for further investigation in the present study.
- The nominal value for the nucleation factor of intra-granular bubbles has been updated relative to [69]. However, the range of variation has been kept the same.
- The nominal values for the U_3Si_2/gas specific surface energy and semi-dihedral angle of inter-granular bubbles have been updated relative to [69], and are based on the recent molecular dynamics calculations in [70]. The variation ranges were adjusted accordingly.
- The nominal value for the saturation coverage of grain boundaries has also been updated. The new value of 0.5 is in line with the accepted value for UO_2 and with recent phase field calculations for U_3Si_2 performed at INL for the present milestone work. The variation range has been kept the same as in [69].
- Uniform distributions were assumed for all fission gas model parameters, following [69].
- Additionally, the uncertainty in the intra-granular diffusion coefficient of gas atoms and vacancies is considered here in that separate calculations are performed for both the stoichiometric and Si-rich U_3Si_2 models (Section 3.5.2).

Table 7: Parameters considered in the sensitivity analysis for U_3Si_2 and corresponding ranges of variation.

Parameter	Nominal value	Scaling factor range	Distribution
Thermal conductivity ($W{\cdot}m^{-1}K^{-1}$)	See Equation 29	[0.82; 1.18]	Normal
Coefficient of thermal expansion (K^{-1})	$16.0{\times}10^{-6}$	[0.8125;1.1875]	Normal
Young's modulus (GPa)	See Equation 39	[0.709; 1.291]	Normal
Shear modulus (GPa)	See Equation 40	[0.732; 1.268]	Normal
Solid swelling (/)	See Equation 68	[0.8; 1.2]	Normal
Nucleation factor of intra-granular bubbles (/)	10^{-6}	$[10^{-3}; 10^{4}]$	Uniform
Re-solution rate of intra-granular bubbles (s^{-1})	$2.80 \cdot 10^{-25} \left(5 \cdot 10^{-10}/R_{ig}\right)^{0.23} \cdot \dot{F}$	[0.1; 10]	Uniform
U_3Si_2/gas specific surface energy ($J{\cdot}m^{-2}$)	1.7	[0.5; 1.5]	Uniform
Inter-granular diffusion coefficient of vacancies ($m{\cdot}s^{-2}$)	$10^{6} \cdot D_{ig}^{v}$	$[10^{-2}; 10^{2}]$	Uniform
Initial number density of inter-granular bubbles ($bbl{\cdot}m^{-2}$)	$2 \cdot 10^{12}$	$[10^{-3}; 10^{3}]$	Uniform
Semi-dihedral angle of inter-granular bubbles (deg)	72.9	[0.5; 1]	Uniform
Saturation coverage of grain boundaries (/)	0.5	$[1; \pi/2]$	Uniform

5.2.2 Results and Discussion: ATF-13 R4

For the sensitivity analysis of U_3Si_2 fuel modeling, the case considered here is the ATF-13 R4 rod (Section 4.2.1). For the reference Bison calculation, the settings are the same as used in the validation study presented in Section 4.2.1.

The results of the sensitivity analysis in terms of Spearman correlation coefficients are presented in Figures 23 and 24. Figure 23 corresponds to the study where the diffusivity models for stoichiometric U_3Si_2 were applied, while Figure 24 is from the analysis using the model for Si-rich U_3Si_2 (Section 3.5.2). Considered figures of merit are integral FGR in the fuel rod and fuel stack elongation, both at the end of life.

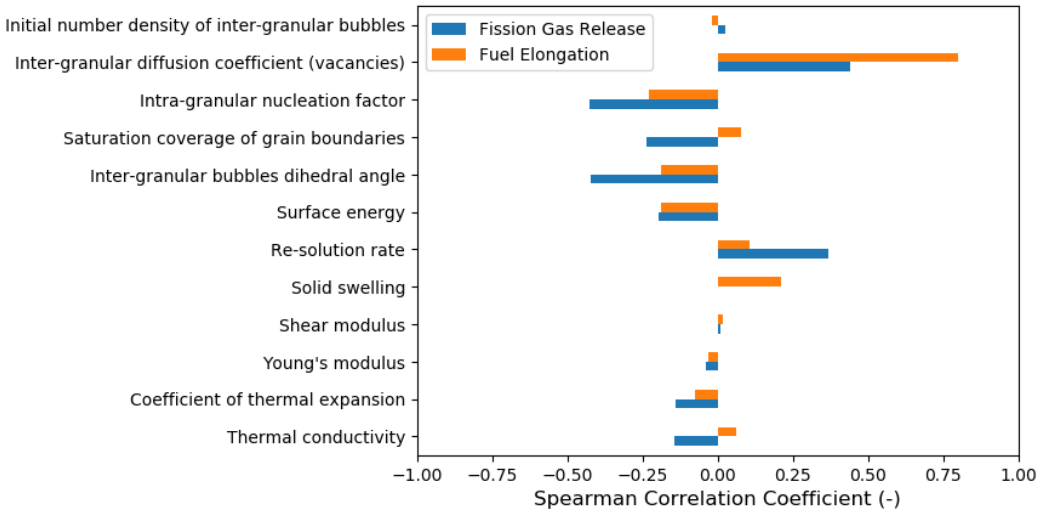

Figure 23: Spearman correlation coefficients for the stoichiometric U_3Si_2 case.

In both cases, the inter-granular diffusion coefficient of vacancies is the parameter that has the largest impact on both FGR and fuel elongation. A faster diffusion of vacancies to inter-granular bubbles favors bubble growth, which results in fuel gaseous swelling, and the eventual FGR after the saturation bubble coverage of grain boundaries is reached (Section 3.5.1). Hence the positive correlation of the vacancy diffusion coefficient to both FGR and fuel elongation. It is noted that the effect of the inter-granular diffusion coefficient of vacancies in this case is markedly higher than observed for the sensitivity analysis of Cr_2O_3-doped UO_2 fuel modeling (Section 5.1). This is potentially associated with the lower FGR observed in this U_3Si_2 case, meaning that the saturation condition for grain boundaries and the onset of FGR are more narrowly reached (or not reached, for some combinations of parameters). This implies that small changes in the parameter lead to large factorial variations of FGR in the U_3Si_2 case.

Other parameters that are strongly correlated to the FGR are the intra-granular nucleation factor, the dihedral angle of inter-granular bubbles, and the re-solution rate. A higher nucleation factor results in a higher number of intra-granular bubbles, which tend to trap gas atoms and therefore to reduce the arrival rate of fission gas atoms to grain boundaries. This ultimately results in a lower FGR. Hence the negative correlation of the nucleation factor with FGR. The correlation of the nucleation factor with gaseous swelling (hence, fuel elongation) is less obvious. A larger number of intra-granular bubbles tends, on the one hand, to reduce gas transport to grain boundaries and inter-granular swelling, on the other, it favors intra-granular swelling, which is also taken into account in the U_3Si_2 fission gas model (Section 3.5.1). The dihedral angle of inter-granular bubbles is negatively correlated to FGR because the attainment of the saturation bubble coverage of grain boundaries is retarded for bubbles with a higher dihedral angle. The re-solution rate from intra-granular bubbles affects the intra-granular diffusion of gas atoms (Eq. 52). In particular, a higher re-solution rate corresponds to a higher rate of gas transport to grain boundaries, which in turn favors FGR (Section 2.4). Hence the positive correlation of the re-solution rate with FGR. Also for the re-solution rate, the effect on gaseous sweling and fuel elongation is less obvious. A higher re-solution favors the swelling due to inter-granular bubbles, but it also counteracts swelling due to intra-granular bubbles as it acts to knock gas atoms from bubbles back into the lattice.

Considering as figures of merit the integral FGR in the fuel rod and fuel stack elongation, both at the end of life, sensitivity analysis results in terms of $\pm 2\sigma$ are reported in Table 8 as part of uncertainty quantification. Both cases with the stoichiometric and Si-Rich U_3Si_2 diffusivity models (see Section 3.5.2) are included. Experimental data are also reported.

In both cases, the variation range of Bison predictions contains the experimental data. Both maximum fuel elongation and FGR are higher in the case of the models for stoichiometric U_3Si_2, which corresponds to the different diffusivities of gas atoms and vacancies in the two cases.

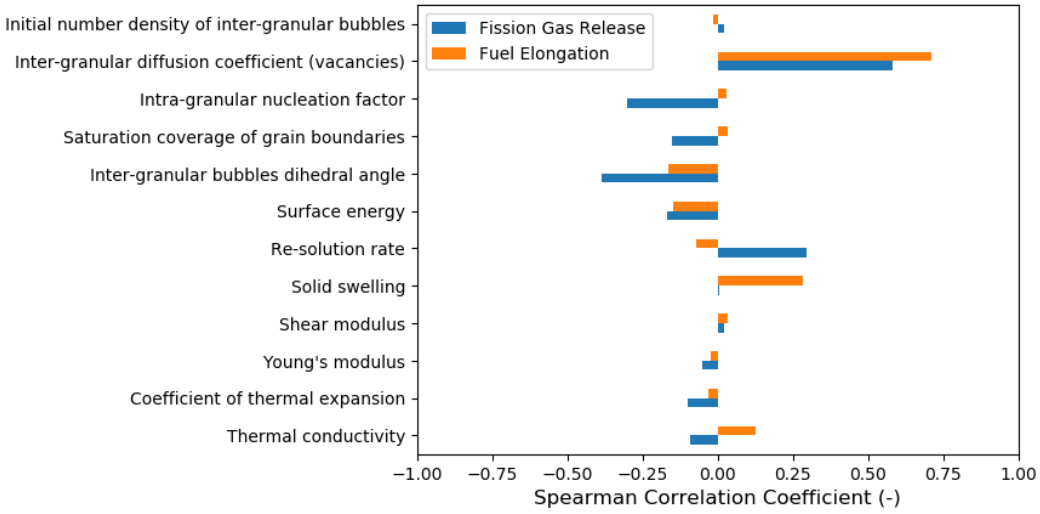

Figure 24: Spearman correlation coefficients for the Si-rich U_3Si_2 case.

Table 8: Bison comparisons to ATF-13 R4 PIE data including $\pm 2\sigma$ for both stoichiometric and Si-Rich diffusivity models.

	Bison Stoichiometric	Bison Si-Rich	Experiment
Fuel Elongation (mm)	-0.135 to 0.132	-0.1305 to 0.0567	0
Fission Gas Release (%)	0.0 to 1.412	0.0 to 0.902	0.06

6 Conclusions

The primary focus of this report was listing the models available in Bison for the priority fuel concepts, Cr_2O_3-doped UO_2 and U_3Si_2 including the range of applicability of the model and an estimation of the uncertainty in model. For empirically based models the uncertainty was derived from the experimental data upon which the model is created. For lower length scale informed models, the uncertainty in lower length scale parameters was propagated up to the engineering scale.

Beyond providing a comprehensive overview of the models in a similar form to NUREG/CR-7024, new validation cases were completed for the Cr_2O_3-doped $UO_2$and U_3Si_2 fuel concepts. The Cr_2O_3-doped UO_2 models were validated against three experiments from the Halden reactor (IFA-677.1 rods 1 and 5, IFA-716.1 rod 1). The U_3Si_2 fuel models were validated against two rods (ATF-1W R4 and R6) that recently underwent post-irradiation examination (PIE) after being irradiated in the Advanced Test Reactor (ATR). Finally, uncertainty quantification and sensitivity analysis were completed on a single validation case for each fuel concept. Select models were sampled within their estimated uncertainty and the effect on the Bison prediction for fuel performance metrics of interest such as fission gas release, fuel temperature, fuel elongation, and rod internal pressure was identified.

The work documented here significantly improves the documentation of modeling capabilities currently available in Bison for fuel performance analyses of the NRC identified priority fuel concepts. Quantification of the uncertainty in the models and the application of the models to validation cases help new users determine which model to use for their analyses involving these fuel concepts.

7 Acknowledgements

This work was funded by the U.S. Department of Energy under the Consortium for Advanced Simulation of Light Water Reactors (CASL) program. The report has been authored by a contractor of the U.S. Government under Contract DE-AC07-05ID14517. Accordingly, the U.S. Government retains a non-exclusive, royalty free license to publish or reproduce the published form of this contribution, or allow others to do so, for U.S. Government purposes. This research made use of the resources of the High Performance Computing Center at Idaho National Laboratory, which is supported by the Office of Nuclear Energy of the U.S. Department of Energy and the Nuclear Science User Facilities under Contract No. DE-AC07-05ID14517.

References

[1] W. G. Luscher and K. J. Geelhood. Material property correlations: Comparisons between FRAPCON-3.5, FRAPTRAN-1.5 and MATPRO. Technical Report NUREG/CR-7024 Rev. 1, United States Nuclear Regulatory Commission, 2014.

[2] F. Cappia and J. M. Harp. Postirradiation examination of low burnup U_3Si_2 fuel for light water reactor applications. *Journal of Nuclear Materials*, 518:62–79, 2019.

[3] M.W.D. Cooper. Data needs and path to doped UO_2 fuel performance modeling. Technical Report M4FT-19LA0202010112, LA-UR-19-24565, Los Alamos National Laboratory, May 2019.

[4] J. Arborelius, K. Backman, L. Hallstadius, M. Limbäck, J. Nilsson, B. Rebensdorff, R. Löfström, and G. Rönnberg. Advanced doped UO_2 pellets in LWR applications. *Journal of Nuclear Science and Technology*, 43:967–976, 2006.

[5] T. Watanabe, S.B. Sinnott, J.S. Tulenko, R.W. Grimes, P.K. Schelling, and S.R. Phillpot. Thermal transport properties of uranium dioxide by molecular dynamics simulations. *Journal of Nuclear Materials*, 375:388–396, 2008.

[6] B. Baurens. In-pile results from the fission gas release mechanisms study in IFA-716 after final unloading. Technical Report HWR-1161, OECD Halden Reactor Project, April 2016.

[7] Incorporation of Chromia-Doped Fuel Properties in AREVA Approved Methods. Technical Report ANP-10340NP, AREVA, April 2016.

[8] J. K. Fink. Thermophysical properties of uranium dioxide. *Journal of Nuclear Materials*, 279(1):1–18, 2000.

[9] D.D. Lanning, C.E. Beyer, and K.J. Geelhood. FRAPCON-3 Updates, Including Mixed-Oxide Fuel Properties. Technical Report NUREG/CR-6534, Vol. 4 PNNL-11513, Pacific Northwest National Laboratory, 2005.

[10] T. Ikonen and V. Tulkki. The importance of input interactions in the uncertainty and sensitivity analysis of nuclear fuel behavior. *Nuclear Engineering and Design*, 275:229–241, 2014.

[11] K. Geelhood, W. Luscher, C. Beyer, D. Senor, M. Cunningham, D. Lanning, and H. Adkins. Predictive bias and sensitivity in NRC fuel performance codes. Technical Report NUREG-CR-7001, Pacific Northwest National Laboratory, 2009.

[12] K. Geelhood, W. Luscher, and C. Beyer. FRAPCON-3.4: A computer code for the calculation of steady-state thermal-mechanical behavior of oxide fuel rods for high burnup. Technical Report NUREG-CR-7022, Vol. 1., Pacific Northwest National Laboratory, 2011.

[13] Thermophysical properties database of materials for light water reactors and heavy water reactors. Final report of a coordinated research project 1999–2005. Technical Report IAEA-TECDOC-1496, June 2006.

[14] K. Une. Thermal Expansion of UO_2-Gd_2O_3 Fuel Pellets. *Journal of Nuclear Science and Technology*, 23(11):3–6, 1986.

[15] A.C. Momin, E.B. Mirza, and M.D. Mathews. High temperature X-ray diffractometric studies on the lattice thermal expansion behaviour of UO_2, ThO_2 and $(U_0.2Th_0.8)O_2$ doped with fission product oxides. *Journal of Nuclear Materials*, 185:308–310, 1991.

[16] C. M. Allison, G. A. Berna, R. Chambers, E. W. Coryell, K. L. Davis, D. L. Hagrman, D. T. Hagrman, N. L. Hampton, J. K. Hohorst, R. E. Mason, M. L. McComas, K. A. McNeil, R. L. Miller, C. S. Olsen, G. A. Reymann, and L. J. Siefken. SCDAP/RELAP5/MOD3.1 code manual, volume IV: MATPRO–A library of materials properties for light-water-reactor accident analysis. Technical Report NUREG/CR-6150, EGG-2720, Idaho National Engineering Laboratory, 1993.

[17] J.B. Ainscough, B.W. Oldfield, and J.O. Ware. Isothermal grain growth kinetics in sintered UO_2 pellets. *Journal of Nuclear Materials*, 49:117–128, 1973.

[18] M.I. Mendelson. Average grain size in polycrystalline ceramics. *Journal of the American Ceramic Society*, 52:443–446, 1969.

[19] P. Van Uffelen, P. Botazzoli, L. Luzzi, S. Bremier, A. Schubert, P. Raison, R. Eloirdi, and M. A. Barker. An experimental study of grain growth in mixed oxide samples with various microstructures and plutonium concentrations. *Journal of Nuclear Materials*, 434:287–290, 2013.

[20] P. Botazzoli. *Helium production and behaviour in LWR nuclear oxide fuels*. PhD thesis, Politecnico di Milano, Italy, 2011.

[21] G. Pastore, L.P. Swiler, J.D. Hales, S.R. Novascone, D.M. Perez, B.W. Spencer, L. Luzzi, P. Van Uffelen, and R.L. Williamson. Uncertainty and sensitivity analysis of fission gas behavior in engineering-scale fuel modeling. *Journal of Nuclear Materials*, 465:398–408, 2015.

[22] M. V. Speight. A calculation on the migration of fission gas in material exhibiting precipitation and re-solution of gas atoms under irradiation. *Nuclear Science and Engineering*, 37:180–185, 1969.

[23] J. A. Turnbull, C. A. Friskney, J. R. Findlay, F. A. Johnson, and A. J. Walter. The diffusion coefficients of gaseous and volatile species during the irradiation of uranium dioxide. *Journal of Nuclear Materials*, 107:168–184, 1982.

[24] J. A. Turnbull, R.J. White, and C. Wise. The diffusion coefficient for fission gas atoms in uranium dioxide. In *Proceedings of Technical Committee Meeting on Water Reactor Fuel Element Computer Modelling in Steady State, Transient and Accident Conditions*, pages 174–181, Preston, UK, Sept. 18–22, 1988.

[25] F. S. Ham. Theory of diffusion-limited precipitation. *Journal of Physics and Chemistry of Solids*, 6:335–351, 1958.

[26] R. J. White and M. O. Tucker. A new fission-gas release model. *Journal of Nuclear Materials*, 118(1):1–38, 1983.

[27] J. A. Turnbull. A review of irradiation induced re-solution in oxide fuels. *Radiation Effects*, 53:243–249, 1980.

[28] M. V. Speight and W. Beere. Vacancy potential and void growth on grain boundaries. *Metal Science*, 9:190–191, 1975.

[29] R. J. White. The development of grain-face porosity in irradiated oxide fuel. *Journal of Nuclear Materials*, 325:61–77, 2004.

[30] G. Pastore, L. Luzzi, V. Di Marcello, and P. Van Uffelen. Physics-based modelling of fission gas swelling and release in UO_2 applied to integral fuel rod analysis. *Nuclear Engineering and Design*, 256:75–86, 2013.

[31] C. Vitanza, U. Graziani, N.T. Fordestrommen, and K.O. Vilpponen. Fission gas release from in-pile measurements. Technical Report HPR-221.10, 1978.

[32] S. Kashibe and K. Une. Effect of additives (Cr_2O_3, Al_2O_3, SiO_2, MgO) on diffusional release of ^{133}Xe from UO_2 fuels. *Journal of Nuclear Materials*, 254:234–242, 1998.

[33] J. C. Killeen. Fission gas release and swelling in UO2 doped with Cr2O3. *Journal of Nuclear Materials*, 88(2-3):177–184, 1980.

[34] C Matthews, R. Perriot, M. W. D. Cooper, C. R. Stanek, and D. A. Andersson. Cluster Dynamics Simulation of Uranium Self-di usion During Irradiation in UO2. *Journal of Nuclear Materials*, submitted, 2019.

[35] L. Bourgeois, Ph Dehaudt, C. Lemaignan, and A. Hammou. Factors governing microstructure development of Cr2O3-doped UO2 during sintering. *Journal of Nuclear Materials*, 297(3):313–326, 2001.

[36] T B Lindemer and T M Besmann. Chemical Thermodynamic Representation of UO2+x. *Journal of Nuclear Materials*, 130:473–488, 1985.

[37] R. L. Williamson, K. A. Gamble, D. M. Perez, S. R. Novascone, G. Pastore, R. J. Gardner, J. D. Hales, W. Liu, and A. Mai. Validating the BISON fuel performance code to integral LWR experiments. *Nuclear Engineering and Design*, 301:232 – 244, 2016.

[38] T. Barani, E. Bruschi, D. Pizzocri, G. Pastore, P. Van Uffelen, R.L. Williamson, and L. Luzzi. Analysis of transient fission gas behaviour in oxide fuel using BISON and TRANSURANUS. *Journal of Nuclear Materials*, 486:96–110, 2017.

[39] G. Pastore, C.P. Folsom, R.L. Williamson, J.D. Hales, L. Luzzi, D. Pizzocri, and T. Barani. Modelling fission gas behaviour with the bison fuel performance code. In *Enlarged Halden Programme Group Meeting, Lillehammer, Norway, September 24-29*, 2017.

[40] Y. Rashid, R. Dunham, and R. Montgomery. Fuel analysis and licensing code: FALCON MOD01. Technical Report EPRI 1011308, Electric Power Research Institute, December 2004.

[41] B. Thérache. The High Initial Rating Test, IFA-677.1: Results after First Cycle of Irradiation. Technical Report HWR-819, OECD Halden Reactor Project, September 2005.

[42] O. Brémont. IFA-716.1 Fission gas release mechanisms. Technical Report HWR-1008, OECD Halden Reactor Project, September 2011.

[43] R. Jošek. The High Initial Rating Test IFA-677: Final Report on In-Pile Results. Technical Report HWR-872, OECD Halden Reactor Project, April 2008.

[44] H. K. Jenssen. PIE Report on Six UO_2 Fuel Rods Irradiated in IFA-677 High Initial Rating Test. Technical Report HWR-968, OECD Halden Reactor Project, March 2010.

[45] T. Tverberg. Update on the in-pile results from the fission gas release mechanisms study in IFA-716. Technical Report HWR-1090, OECD Halden Reactor Project, September 2014.

[46] A.G. Evans and R.W. Davidge. The strength and fracture of stoichiometric polycrystalline UO_2. *Journal of Nuclear Materials*, 33:249–260, 1969.

[47] M. Oguma. Microstructure Effects on Fracture Strength of UO2 Fuel Pellets. *Journal of Nuclear Science and Technology*, 19:1005–1014, 1982.

[48] T. Barani, D. Pizzocri, G. Pastore, L. Luzzi, and J.D. Hales. Isotropic softening model for fuel cracking in BISON. *Nuclear Engineering and Design*, 342:257–263, 2019.

[49] C. Nonon, J. Menard, S. Lansiart, J. Noirot, S. Martin, G. Decroix, O. Rabouille, C. Delafoy, and B. Petitprez. PCI behaviour of chromium oxide doped fuel. In *International Seminar on Pellet-Clad Interaction in Water Reactor Fuels, OECD-NEA, Aix-en Provence, France, 9-11*, page 305, 2004.

[50] J. T. White, A. T. Nelson, J. T. Dunwoody, D. J. Safarik, and K. J. McClellan. Corrigendum to Thermophysical Properties of U_3Si_2 to 1773 K. *Journal of Nuclear Materials*, 484:386–387, 2017.

[51] J. T. White, A. T. Nelson, J. T. Dunwoody, D. D. Byler, D. J. Safarik, and K. J. McClellan. Thermophysical properties of U_3Si_2 to 1773K. *Journal of Nuclear Materials*, 464:275–280, 2015.

[52] H. Shimizu. The properties and irradiation behavior of U_3Si_2. Technical Report NAA-SR-10621, Atomics International, 1965.

[53] K. E. Metzger, T. W. Knight, and R. L. Williamson. Model of U_3Si_2 fuel system using BISON fuel code. In *Proceedings of the International Congress on Advances in Nuclear Power Plants - ICAPP 2014*, Charlotte, NC, April 6–9 2014.

[54] C.Y. Ho, M.W. Ackerman, K.Y. Wu, S.G. Oh, and T.N. Havill. Thermal conductivity of ten selected binary alloy systems. *Journal of Physical and Chemical Reference Data*, 7:959, 1978.

[55] Yu. Tsiovkin, V.V. Dremov, E.S. Koneva, A.A. Povzner, A.N. Filanovich, and A.N. Petrova. Theory of the residual electrical resistivity of binary actinide alloys. *Journal of Physics of the Solid State*, 52:1–5, 2010.

[56] C.J. Glassbrenner and G.A. Slack. Thermal conductivity of silicon and germanium from 3k to the melting point. *Journal of Physical Review*, 134:A1059, 1964.

[57] J. T. White, A. T. Nelson, D. D. Byler, D. J. Safarik, J.T. Dunwoody, and K. J. McClellan. Thermophysical properties of U_3Si_5 to 1773K. *Journal of Nuclear Materials*, 456:442–448, 2015.

[58] J. T. White. Update to the U_3Si_2 property handbook. Technical Report LA-UR-18-28719, Los Alamos National Laboratory, 2018.

[59] A. Mohamad, Y. Ohishi, H. Muta, K. Kurosaki, and S. Yamanaka. Thermal and mechanical properties of polycrystalline U_3Si_2 synthesized by spark plasma sintering. *Journal of Nuclear Science and Technology*, 55(10):1141–1150, 2018.

[60] D. Antonio, K. Shrestha, J. Harp, C. Adkins, Y. Zhang, J. Carmack, and K. Gofryk. Thermal and transport properties of U_3Si_2. *Journal of Nuclear Materials*, 508:154–158, 2018.

[61] Y. Miao, K. A. Gamble, D. Andersson, B. Ye, Z. Mei, G. Hofman, and A. M. Yacout. Gaseous swelling of U_3Si_2 during steady-state lwr operation: A rate theory investigation. *Nuclear Engineering and Design*, 322:336–344, 2017.

[62] J. E. Matos and J. L. Snelgrove. Research reactor core conversion guidebook-Vol 4: Fuels (Appendices I-K). Technical Report IAEA-TECDOC-643, IAEA, 1992.

[63] J. T. White. Issue draft U_3Si_2 fuel property handbook. Technical Report LA-UR-17-20609, Los Alamos National Laboratory, 2017.

[64] K. M. Taylor and C. H. McMurtry. Synthesis and fabrication of refractory uranium compounds: Summary report for may 1959 through december 1960. Technical Report ORO-400, 1961.

[65] U. Carvajal-Nunez, T. Saleh, J. White, B. Baiorov, and A. Nelson. Determination of elastic properties of polycrystalline U_3Si_2 using resonant ultrasound spectroscopy. *Journal of Nuclear Materials*, 498:438–444, 2018.

[66] R. A. Freeman, T. Martin, E. Roberts, and T. W. Knight. Analysis of thermal creep for uranium silicide fuel using Bison. In *Proceedings of the 2018 International Congress on Advances in Nuclear Power Plants (ICAPP 18)*, Charlotte, NC, 2018.

[67] K. E. Metzger. *Analysis of Pellet Cladding Interaction and Creep of U_3Si_2 Fuel for use in Light Water Reactors*. PhD thesis, University of South Carolina, 2016.

[68] L. D. Loch, G. B. Engle, M. J. Snyder, and W. H. Duckworth. Survey of refractory uranium compounds. Technical Report BMI-1124, Battelle Memorial Institute, 1956.

[69] T. Barani, G. Pastore, D. Pizzocri, D.A. Andersson, C. Matthews, A. Alfonsi, K.A. Gamble, P. Van Uffelen, L. Luzzi, and J.D. Hales. Multiscale modeling of fission gas behavior in U_3Si_2 under LWR conditions. *Journal of Nuclear Materials*, 522:97–110, 2019.

[70] B. Beeler, M. Baskes, D. Andersson, M.W.D. Cooper, and Y. Zhang. Molecular dynamics investigation of grain boundaries and surfaces in U_3Si_2. *Journal of Nuclear Materials*, 514:290–298, 2019.

[71] G. Pastore, D. Pizzocri, C. Rabiti, T. Barani, P. Van Uffelen, and L. Luzzi. An effective numerical algorithm for intra-granular fission gas release during non-equilibrium trapping and resolution. *Journal of Nuclear Materials*, 509:687–699, 2018.

[72] D A Andersson, X Liu, B Beeler, S C Middleburgh, A Claisse, and C R Stanek. Density functional theory calculations of self- and Xe diffusion in U3Si2. *Journal of Nuclear Materials*, 515:312–325, 2019.

[73] M W D Cooper, C R Stanek, J A Turnbull, B P Uberuaga, and D A Andersson. Simulation of radiation driven fi ssion gas diffusion in UO 2 , ThO 2 and PuO 2. *Journal of Nuclear Materials*, 481:125–133, 2016.

[74] Benjamin Beeler, M. I. Baskes, D. A. Andersson, M. W. D. Cooper, and Yongfeng Zhang. A modified Embedded-Atom Method interatomic potential for uranium-silicide. *Journal of Nuclear Materials*, 495:267–276, 2017.

[75] G. L. Hofman and W. S. Ryu. Detailed Analysis of Uranium Silicide Dispersion Fuel Swelling. Technical Report CONF-8909141–10, Argonne National Laboratory, 1989.

[76] J.L Snelgrove M. R. Finlay, G. L. Hofman. Irradiation behaviour of uranium silicide compounds. *Journal of Nuclear Materials*, 325:118–128, 2004.

[77] K. Lassmann, A. Schubert, J. van de Laar, and P. Van Uffelen. The 'Fuel Rod Analysis ToolBox': a general program for preparing the input of a fuel rod performance code. *Annals of Nuclear Energy*, 81:332–335, 2015.

[78] W. Wiesenack. Verification and improvement of test data for the HRP Legacy Data Base. In *Enlarged Halden Programme Group Meeting, Sandefjord, Norway, May 19–24*, 2019.

[79] Fuel Modelling in Accident Conditions (FUMAC): Report of a Coordinated Research Project (CRP T12028) 2014–2018. Technical report, International Atomic Energy Agency. In preparation.

[80] K. E. Barrett, K. D. Ellis, C. R. Glass, G. A. Roth, M. P. Teague, and J. Johns. Critical processes and parameters in the development of accident tolerant fuels drop-in capsule irradiation tests. *Nuclear Engineering and Design*, 294:38–51, 2015.

[81] J. M. Harp, P. A. Lessing, and R. E. Hoggan. Uranium silicide pellet fabrication by powder metallurgy for accident tolerant fuel evaluation and irradiation. *Journal of Nuclear Materials*, 466:728–738, 2015.

[82] F. Cappia and J. M. Harp. Corrigendum to "postirradiation examination of low burnup U_3Si_2 fuel for light water reactor applications". *Journal of Nuclear Materials*, 523:538, 2019.

[83] B. M. Adams, L. E. Bauman, W. J. Bohnhoff, K. R. Dalbey, M. S. Ebeida, J. P. Eddy, M. S. Eldred, P. D. Hough, K. T. Hu, J. D. Jakeman, J. A. Stephens, L. P. Swiler, D. M. Vigil, and T. M. Wildey. Dakota, a multilevel parallel object-oriented framework for design optimization, parameter estimation, uncertainty quantification, and sensitivity analysis: Version 6.0 user's manual. Technical Report SAND2014-4633 Version 6.3, Sandia National Laboratories, 2015.